The oxygen evolution reaction mechanism at $Ir_xRu_{1-x}O_2$ powders produced by hydrolysis synthesis

Anita Hamar Reksten[1], Heidi Thuv[2], Frode Seland[2], Svein Sunde[2,*]

Department of Materials Science and Engineering, Norwegian University of Science and Technology (NTNU), NO-7491 Trondheim, Norway.

Abstract

A mechanistic study of the oxygen evolution reaction (OER) has been performed for $Ir_xRu_{1-x}O_2$, x=1, 0.6, 0.3 and 0, prepared by the hydrolysis synthesis. The oxides were characterized by X-ray diffraction, cyclic voltammetry and steady state polarization measurements. The electrolyte pH was varied in order to study the reaction order with respect to protons. The polarization curves recorded could be well fitted to a model consisting of a series of concerted electron-proton transfer reactions (mononuclear mechanism) with either of the second, third, or fourth step being rate determining. The expected trends for this mechanism with respect to potential and pH were observed in the experimental data and are consistent with DFT results for the adsorption energies of the adsorbates [Rossmeisl *et al.*, *J. Electroanal. Chem.* **607** (2007) 83 – 89] if the third or fourth step is rate-determining for RuO_2 and IrO_2, respectively.

The fitting procedures also demonstrate the advantages of working with the full current-voltage expression when analyzing polarization curves, since Tafel behaviour may only prevail in a limited potential region.

Keywords: electrocatalysis, reaction order, water oxidation, iridium oxide, ruthenium oxide
2010 MSC: 00-01, 99-00

1. Introduction

The proton exchange membranes (PEM) water electrolyzer [1] is today considered to play a role in the integration of renewable energy sources. Conversion of electricity into the energy storage medium hydrogen gas can be conveniently and efficiently carried out in PEM water electrolyzers. Production of hydrogen by water electrolysis is traditionally carried out by alkaline water electrolysis (WE) which has an established technology and is widely used in the industry. However, PEM water electrolysis (WE) offers some advantages over alkaline WE, such as higher efficiency, higher current density, more compact design, can be operated under fluctuating current input and has higher purity of the hydrogen gas [2].

Critical to any efficient water electrolysis design are active catalysts for the anode and cathode reactions. Catalyst activities are frequently ranked in terms of the Sabatier principle and so-called volcano curves, as outlined by Parsons [3]. According to the Sabatier principle bonding is necessary for reactions (involving adsorbed intermediates) to proceed, but too strong bonding will block the surface [3]. The rate of an electrochemical reaction at a given potential is thus expected to depend on the binding energy of adsorbates, and the surface should bind these neither too weakly nor too strongly. The volcano curve correlates the bond strength of key adsorbed intermediates to the activity of the catalyst with respect to a certain reaction, and is usually shaped as the name implies as a volcano. For the hydrogen evolution reaction a volcano relationship thus exists between the activity of the catalyst and the bond strength of hydrogen to the metal surface [3], with Pt appearing close to the apex of the volcano.

*Corresponding author. Tel.: +47 735 94051; fax: +47 73 59 11 05
Email address: svein.sunde@ntnu.no (Svein Sunde)
[1]*Current address:* Institute for Energy Technology(IFE), Instituttv. 18, NO-2007 Kjeller, Norways
[2]ISE member

Similar relations have been proposed for the oxygen-evolution reaction (OER) in terms of the binding energy of oxygen at the surface. Rüetschi and Delahay [4] correlated the overpotential for the OER on metal electrodes in alkaline solutions with the binding energy for OH. For oxide OER catalysts Trasatti [5] suggested correlating the overpotential with the enthalpy associated with the transition $MO_x \rightarrow MO_{1+x}$, generally referred to as the "lower → higher oxide transition" and in which MO_x and MO_{1+x} are two forms of the oxide differing in the ratio between the metal (M) to oxygen content ($1 : x \rightarrow 1 : 1 + x$). Trasatti [5] was thus able to obtain a volcano-shaped curve for the catalytic activity of a number of oxides vs the enthalpy of the lower → higher oxide transition with RuO_2. More recent correlations have been proposed by Rossmeisl *et al.* [6], who established a volcano curve for the OER for oxides in terms of the binding energy for oxygen at oxide surfaces based on density functional theory (DFT) calculations, and Suntivich *et al.* [7] who based their volcano on the number of d-electrons in the catalyst.

The highly acidic environment required by the membrane in the PEM imposes tough criteria for the materials used in PEM water electrolysis technology. Only a small selection provides sufficient stability. The catalysts, on both anode and cathode, are therefore often based on noble metals such as Pt and Ir [8], which in addition to providing efficient catalysis also display the necessary durability. The catalysts exhibiting the highest activity towards oxygen evolution reaction (OER) are RuO_2 and IrO_2, ruthenium oxide being more active than iridium oxide, but also more unstable. Mixing of these two oxides is therefore often performed in order to achieve both an active and stable catalyst [9, 10, 11].

The prediction of catalytic activity is thus central to rational design of catalysts, implying, in view of the above, that reaction mechanisms should be known in order to identify the adsorbates whose binding energy determine the catalyst activity. However, a complete understanding of the oxygen evolution reaction, or its reduction counterpart the oxygen reduction reaction (ORR), has not been obtained, and a range of mechanisms describing the OER have been suggested [6, 12, 13]. So-called scaling relations between adsorbates based on DFT relations simplify the task of establishing binding energy-activity correlations by introducing correlations between the binding energies of different possible adsorbates in a reaction mechanism [14, 15]. However, verification of the predictions of these theories experimentally in terms of mechanism, for example through careful interpretation of the potential and pH-dependence of reaction rates, is invaluable in efforts towards a rational design of electrocatalysts for PEM water electrolysis.

The scaling relations represent a severe limitation to the design of efficient electrocatalysts for mechanisms with more than one adsorbate, since for a homogeneous set of catalytic sites one cannot change the binding energy of one adsorbate without changing that of all the others at the same time. This leads to the notion of the "thermodynamic overpotential", i.e the minimum potential required to bring all the steps of reaction thermodynamically downhill, frequently formulated for mechanisms consisting of a series of ion-coupled electron transfer reactions [6, 16, 17, 18]. In this case the thermodynamic overpotential is minimized when the equilibrium potentials of all the steps are equal to the overall equilibrium potential [6, 19]. To overcome this limitation one may devise structurally [20] or chemically heterogeneous catalysts [17]. Another alternative, suggested by Koper [19], is to change the path altogether. Thus, decoupled proton-electron pathways give reaction intermediates different from those consisting exclusively of concerted proton-electron transfer [19]. For decoupled pathways the thermodynamic volcano curves become dependent on pH [19]. However, possibilities for discrimination of the different coupled and decoupled pathways need careful scrutiny from the point of view of experimental determination.

It is thus the purpose of this paper to address the potential and pH-dependence of $Ir_{1-x}Ru_xO_2$ of four different compositions (including the end members) from the point of view of an ensemble of reaction mechanisms containing concerted and decoupled proton-electron transfer reactions. Rather than inferring the reaction orders and potential dependence independently we will fit the polarization curves to model expressions, and discuss the possible interpretation and ambiguities in the assignment to specific reaction mechanisms and rate-limiting processes. We will do so in terms of recently proposed reaction patterns [21] as well as some older ones. The formulation of models will be done in compliance with definitions and recommendations as outlined by Parsons [22, 23].

In some previous studies in our group [10, 24, 25] the experimentally obtained polarization curves were fitted and Tafel slopes determined by adding a term to correct for ohmic drop assumed to be due to gas evolution, described by Eq. (1)

$$E = a + b \ln i + iR_\Omega \tag{1}$$

Here R_Ω is the ohmic resistance, b is the Tafel slope[3], a is the intercept with the potential-axis and i the charge-normalized current density. A resistance due to gas formation covering the electrode was suggested to partly be the cause of the upwards bending, which typically is a feature of polarization curves recorded for these material systems. The resistance was assumed to be approximately constant in a certain potential range beyond the lower linear region, and allowed for an expansion of that region to higher potentials. However, this feature of the experimental current-voltage relationships has persisted, despite extensive attempts to minimize the gas evolution problem and blockage of the electrode, for example by increasing forced convection (wall-jet cells [24] and rotation). At some critical potential the gas evolution will undoubtedly affect the measurements. However, as will be shown below, the procedure implied by Eq. (1) [10, 24, 25] presumably under-utilizes the kinetic information in the data. While providing representative Tafel parameters and sufficient information for the purposes in e.g. Ref [10, 24, 25], Eq. (1) proved inadequate for the present analysis of the pH dependence of OER kinetic data. Hence we have expanded the analysis here to allow for a consistent interpretation over the pH range investigated. In what follows, the upwards bending of the polarization curve is therefore treated rather as a transition to and development of a second Tafel slope in the higher potential range, which is expected for some OER mechanisms and rate-determining steps (rds).

For the synthesis series presented in this work the preliminary analysis based on Eq. (1) indicated that the electrochemical oxide path (or any other mechanism having the same two first reaction steps) with the oxidation of adsorbed hydroxyl ions being the *rds* are the appropriate mechanism and *rds*, respectively, for this system. Using these results as guidelines we analyze kinetic data for powders of $Ir_{1-x}Ru_xO_2$ produced by the hydrolysis method below. The analysis was performed in terms of equations for the current-voltage characteristics expanded to include both high- and low-potential Tafel regions, as well as the transition between the two. A number of mechanisms was included in the analysis, as referred to above. We also demonstrate the inadequacy of some other models that might in a more cursory analysis be suggested to apply. In this way it could be verified that the same proposed mechanism is an appropriate description in more or less the full potential, pH- and compositional range investigated here.

2. Experimental

Synthesis

$Ir_xRu_{1-x}O_2$ powders with x=1, 0.6, 0.3 and 0 were prepared by hydrolysis synthesis. The mixed oxides with iridium fraction of 0.3 and 0.6 will be referred to as Ir30 and Ir60, respectively, below. A 0.5 mol dm^{-3} NaOH (Aldrich ACS reagent > 97%) solution was prepared in a Teflon beaker and heated to 80 °C during continuous stirring. The metal precursors, H_2IrCl_6 $4H_2O$ (Alfa Aesar 99%) and $RuCl_3$ xH_2O (Alfa Aesar PMG basis 99.9%), were dissolved in 10 mL of water before being added to the sodium hydroxide solution. The molar ratio of metal to NaOH was 1:20, and the precursor concentration was in total 0.01 mol dm^{-3}. Stirring of the solution was continued for 1 h at 80 °C. Then, cooling to room temperature followed before the pH was adjusted to 8 by dropwise addition of 1 mol dm^{-3} nitric acid (Merck, pro analysi, Aldrich 69% Puriss). The solution was transferred to a glass beaker and heated while being stirred at 80 °C for 0.5 h before the precipitate was separated and washed in deionized water (Millipore Direct-Q3 18.2 MΩ cm) by centrifugation. The obtained powders were dried in air at 80 °C before they were manually ground with a mortar and pestle. Finally the powders were heat treated for 0.5 h at 500 °C under synthetic air flow in a tube furnace, followed by cooling and additional grinding.

X-ray powder diffraction and Rietveld refinement

XRD measurements for all powders were performed with use of Bruker D8 Focus using Cu K-α radiation. Zero-background silicon sample holders were used. Rietveld analysis was carried out using the Bruker AXS TOPAS version 4.2, using a pseudo-Voigt function. The background intensity was accounted for using a Chebychev polynomial of the order six to account for the curvature. Refinements of diffraction patterns within space group 136 (P42/mnm) were carried out in order to obtain the unit cell values and the crystallite size. The occupancies were set to nominal values, and were not refined.

[3] In the balance of this work we will state Tafel slopes defined by logarithms to base 10.

Electrochemical characterization

The electrodes were prepared similarly to the thin film technique [26]. An ink of the catalyst powder and water was prepared by dissolving the powder in deionized water adjusted to pH 2 with sulfuric acid (1 mg mL^{-1}) with an ultrasonic bath. 20 μL of the ink was pipetted onto a gold RDE with diameter 5 mm (Pine). Any use of Nafion® or other binders was avoided in order eliminate additional pH effects caused by adding these. The ink was dried under a gas steam of N_2. Prior to the ink coating, the gold disc was polished to a mirror finish starting with 5 μm and ending with 0.05 μm alumina paste before being thoroughly rinsed in deionized water and ethanol.

The electrochemical measurements were performed with $HClO_4$ (Merck, pro analysi) solution. The rate of the OER in $HClO_4$ is approximately one order of magnitude higher than in solutions of sulfuric or phosphoric acid [27], and influence of the anion adsorption will therefore be minimal in these solutions. Measurements were carried out at four different pH values. The nominal pH values of the electrolytes were 0, 1, 2 and 3. Constant ionic strength and an approximate constant activity was obtained by the addition of $NaClO_4$ (Aldrich, ACS reagent > 98.0%) to solutions of pH value higher than 0, y mol dm^{-3} $HClO_4$ and $(1-y)$ mol dm^{-3} $NaClO_4$ was used to make the electrolyte solutions, with y equal 1, 0.1, 0.01 and 0.001. The pH of the four solutions were measured with a pH-meter (PHM210, Radiometer Analytical) using a Red Rod pH electrode (Radiometer Analytical, REF201, sat. KCl) and calibrating the pH-meter with buffer solutions of pH 1.09 and pH 4.65 (Radiometer Analytical, Technical grade). The lowest pH did not fit in the range of buffer solutions for calibration and would demonstrate the largest error of the four. The values were found experimentally to be 0.10, 0.96, 1.95 and 2.97 by this procedure.

All electrolyte solutions were prepared with deionized water (Millipore Direct-Q3 18.2 MΩ cm). The reference electrode (RE) used was Ag/AgCl electrode (Radiometer Analytical, REF321) in a 3.0 mol dm^{-3} KCl (Merck, pro analysi 99.5%) solution which eliminated the liquid junction potential between this solution and the inner solution of this RE. The RE was separated from the working electrode compartment by a salt bridge filled with an agar gel (VWR, technical grade) saturated with KNO_3 (Merck, pro analysi). A high concentration of ions with almost similar mobility (76.2×10^{-9} m^2 $V^{-1}s^{-1}$ for K^+ and -74.0×10^{-9} m^2 $V^{-1}s^{-1}$ for NO_3^- at infinite dilution [28]) were employed in order to reduce the liquid junction potential between the two compartments as much as possible. The liquid junction potentials were estimated to be in the order of 1 mV from the Henderson equation [29] for pH 1, 2, and 3. For pH 0 the estimate was 16 mV for which all measurements at this pH were corrected. The tip of the salt bridge was placed in the same height as the WE and as close to the latter as possible, however ~ 2 cm away from the WE due to geometrical constraints. The reference electrode potential was converted to the standard-hydrogen electrode (SHE) scale, and the potentials below are stated with respect to the SHE. The counter electrode was a platinum foil placed vertically on the opposing side of the WE with respect to the RE. A Biologic VMP3 potentiostat was used for all the electrochemical measurements. The rotation of the RDE was controlled with a Pine AFMSRX rotator.

Prior to the polarization measurements all samples were cycled from 0 through 1.4 V at a sweep rate of 350 mV s^{-1} until a stable voltammogram was achieved. The samples were then cycled five times at sweep rates 20, 10, 100, 200, 20, 150, 50, 350, and 20 mV s^{-1} for charge normalization with respect to the outer charge, as described by Ardizzone [30]. Voltammograms at 20 mV s^{-1} were recorded in between the other sweep rates to verify a stable voltammetric response. A fresh sample was used for every pH.

The ohmic resistance was evaluated by a built-in routine in Biologic, using a high frequency potential modulation at 1.35 V before the polarization curve was recorded. 85% of the this ohmic resistance was compensated for during measurements. The polarization curves were recorded through linear sweep voltammetry (LSV) with a sweep rate of 5 mV min^{-1} from 1.35 V vs. SHE while the RDE was rotated at 1800 rpm. After recording the polarization curves cyclic voltammetry at 350 mV s^{-1} (20 cycles) and 20 mV s^{-1} (5 cycles) was performed to assess the stability of the oxide.

The numerical curve fitting of the polarization curves was carried out using Matlab [31] with a Levenberg-Marquardt routine [32].

3. Models for the pH and potential dependence of the OER rate

3.1. A general unimolecular reaction mechanism

As a basis for delineating reaction mechanisms consistent with the pH and potential dependence of the OER rate we consider the unimolecular reaction mechanisms in **Scheme I** below. We have excluded any doubly charged

adsorbates at the surface from our consideration, as indicated by their grey colour in the scheme. The scheme consists of proton transfer steps (which we will denote P in this work) indicated by horizontal arrows, electron transfer steps (E) indicated by vertical arrows, and concerted proton-electron transfer steps (C) [19] indicated by the diagonal arrows. A_{ad} in the scheme indicates a species A bound to a surface site, which are implicit in the notation. Possbilities for limiting the number of possible mechanisms within **Scheme I** and conforming to the experimental data will be discussed towards the end of the paper.

The numbers listed to the far left are the minimum possible Tafel slope for the OER if one of the steps in the same row in the scheme is rate-determining. The slopes are stated as the number of millivolts per decade of current density. The slopes were deduced from Eq. (32) below and coincide with those obtained from the stoichiokinetic equation [33, pp. 130 – 144] for the corresponding reaction mechanism and assuming a charge-transfer coefficient $\alpha = 0.5$. The maximum possible reaction order with respect to protons, $\Omega_{ox,\,H^+}$, also deduced from Eq. (32) below and coinciding with those from the stoichiokinetic equation, are given below the scheme for each of the steps above it being rate-determining.

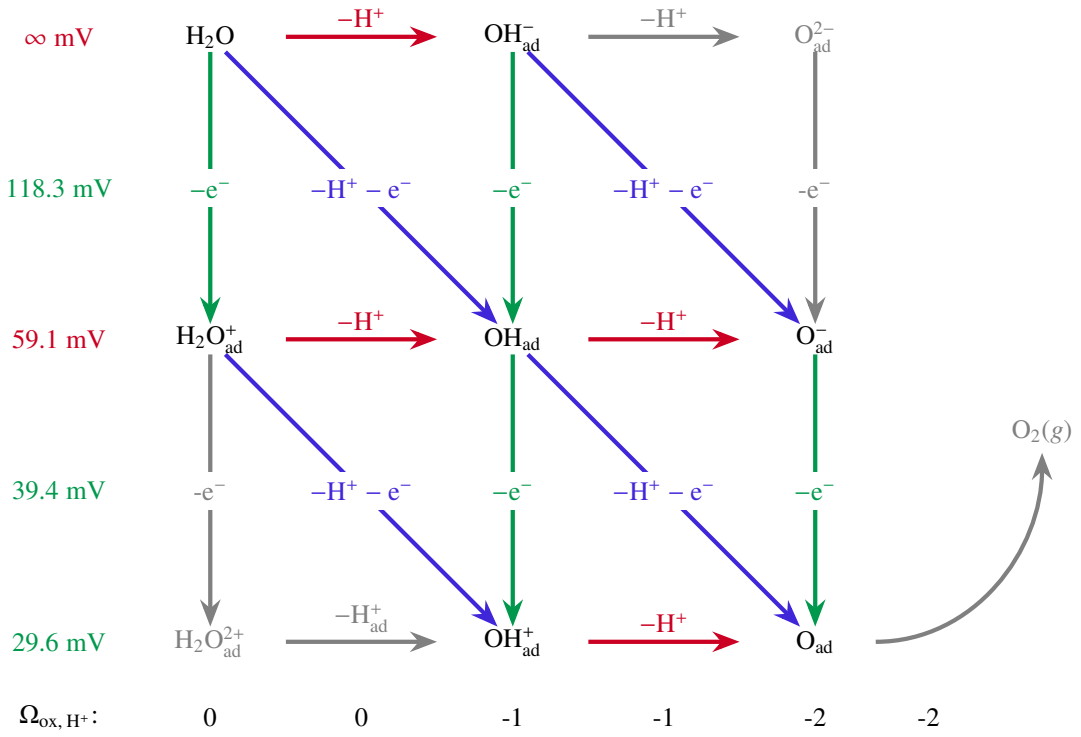

Scheme I

The reaction mechanism in **Scheme I** corresponds to the upper left part of the scheme given by Giordano *et al.* [21, Fig. 2].

The mononuclear path proposed by Rossmeisl *et al.* [6] consisting of steps

$$\mathrm{H_2O}(\ell) \underset{k_{-1}}{\overset{k_1}{\rightleftharpoons}} \mathrm{OH_{ad}} + \mathrm{H^+(aq)} + \mathrm{e^-} \tag{2}$$

$$\mathrm{OH_{ad}} \underset{k_{-2}}{\overset{k_2}{\rightleftharpoons}} \mathrm{O_{ad}} + \mathrm{H^+(aq)} + \mathrm{e^-} \tag{3}$$

$$\mathrm{O_{ad}} + \mathrm{H_2O}(\ell) \underset{k_{-3}}{\overset{k_3}{\rightleftharpoons}} \mathrm{OOH_{ad}} + \mathrm{H^+(aq)} + \mathrm{e^-} \tag{4}$$

$$\mathrm{OOH_{ad}} \underset{k_{-4}}{\overset{k_4}{\rightleftharpoons}} \mathrm{(O_2)_{ad}} + \mathrm{H^+(aq)} + \mathrm{e^-} \tag{5}$$

$$\mathrm{(O_2)_{ad}} \underset{k_{-5}}{\overset{k_5}{\rightleftharpoons}} \mathrm{O_2(g)}, \tag{6}$$

where k_i are rate constants, may serve as an example of a reaction mechanism within the scheme given by Giordano *et al.* [21, Fig. 2], of which the two first are included in **Scheme I** here. (The two last reactions were originally written as one in Ref. [6], but have been written as separate reactions here in order to bring the mechanism in compliance with Ref. [21] and also the reactions to follow in the next section. This difference will be of no consequence here.)

We will indicate below any reaction pattern implied by **Scheme I** by letters indicating the sequence in which the reaction steps appear, each ending with the *rds* since the very assumption of an *rds* implies that reactions subsequent to the *rds* will influence neither reaction orders nor Tafel slopes.

In addition to the unimolecular reaction mechanisms implied by **Scheme I** above we include also an example of a bimolecular mechanism, the oxide path [12, 13].

3.2. Rate expressions for Scheme I

We now consider a general reaction mechanism consisting of a total number of r steps,

$$s_i\mathrm{H_2O} + (\mathrm{O_{a_{i-1}}H_{b_{i-1}}})^{z_{i-1}}_{\mathrm{ad}} \rightleftharpoons (\mathrm{O_{a_i}H_{b_i}})^{z_i}_{\mathrm{ad}} + p_i\mathrm{H^+}(aq) + n_i\mathrm{e^-} \tag{7}$$

$$(\mathrm{O_2})_{\mathrm{ad}} \rightleftharpoons \mathrm{O_2}(g) \tag{8}$$

where $p_i = 0$ or 1 and $n_i = 0$ or 1 and with

$$s_1 = 1 \tag{9}$$

$$a_1 = 0 \tag{10}$$

$$b_1 = 0 \tag{11}$$

$$a_i = a_{i-1} + s_i \tag{12}$$

$$b_i = b_{i-1} + 2s_i - p_i \tag{13}$$

$$z_i = z_{i-1} - p_i + n_i \tag{14}$$

$$a_{r-1} = 2 \tag{15}$$

$$b_{r-1} = 0 \tag{16}$$

$$z_{r-1} = 0 \tag{17}$$

for the first $r - 1$ steps. Eqs. (7) and (8) correspond to **Scheme I** and its extension to the complete scheme as given in Giordano *et al.* [21]. The rate constants for the $r - 1$ first steps are

$$k_i = k_i^0 \exp\left[(1-\alpha_i)\, n_i F \left(E - E^0\right)/RT\right] \tag{18}$$

$$k_{-i} = k_{-i}^0 \exp\left[-\alpha_i n_i F \left(E - E^0\right)/RT\right] \tag{19}$$

where k_i^0 and k_{-i}^0 are constants, α_i are charge-transfer coefficients, E the electrode potential, E^0 the formal electrode potential, F the Faraday's constant, R the gas constant, and T the temperature. We assume that all steps up to the *rds*, which we take to be step $q + 1$, are in quasi-equilibrium, and we define the coverages of all adsorbates as θ_i, the index

referring to the reaction step in which they were generated. We also assume all $\theta_i \approx 0 \; \forall i > q$, i.e. fractional coverages of all species generated downstream of the *rds* are negligible. For the first step we write

$$k_1 \left(1 - \sum_{i=1}^{q} \theta_i \right) = k_{-1} \theta_1 a_{\mathrm{H^+}}^{p_1} \tag{20}$$

For steps $2 \ldots q$ we write (assumption of quasi-equilibrium)

$$\theta_{i-1} = K_i' \theta_i \tag{21}$$

with

$$K_i' = a_{\mathrm{H^+}}^{p_i} \frac{k_{-i}^0}{k_i^0} \exp\left[-n_i F \left(E - E^0 \right) / RT \right] = K_i a_{\mathrm{H^+}}^{p_i} \exp\left[-n_i F \left(E - E^0 \right) / RT \right] \tag{22}$$

For $i = 2$ Eq. (21) may be written

$$\theta_1 = K_2' \theta_2 \tag{23}$$

and for $i = 3$

$$\theta_2 = K_3' \theta_3 \tag{24}$$

Substituting Eq. (24) into Eq. (23) gives

$$\theta_1 = K_2' K_3' \theta_3 \tag{25}$$

We thus obtain by repeated substitution a formula for θ_i

$$\theta_i = \theta_q \prod_{j=i+1}^{q} K_j' \tag{26}$$

Substitution of Eq. (26) into Eq. (20), ignoring all $\theta_{q+1} \ldots \theta_{r-1}$, gives

$$\left[1 - \left(1 + \sum_{i=1}^{q-1} \prod_{j=i+1}^{q} K_j' \right) \theta_q \right] = K_1' \left(\prod_{j=2}^{q} K_j' \right) \theta_q \tag{27}$$

Solved for θ_q this gives

$$\theta_q = \frac{1}{K_1' \left(\prod_{j=2}^{q} K_j' \right) + \left(1 + \sum_{i=1}^{q-1} \prod_{j=i+1}^{q} K_j' \right)} \tag{28}$$

As an example of the application of Eq. (28), for the CCCC mechanism, for which $q = 3$, $p_i = 1 \; \forall i = 1 \ldots q$, and $n_i = 1 \; \forall i = 1 \ldots q$, we obtain

$$\theta_q = \frac{1}{1 + K_1' K_2' K_3' + K_2' K_3' + K_3'} \tag{29}$$

which gives

$$\theta_q = \frac{1}{1 + K_1 K_2 K_3 a_{\mathrm{H^+}}^3 \exp\left[-3F \left(E - E^0 \right) / RT \right] + K_2 K_3 a_{\mathrm{H^+}}^2 \exp\left[-2F \left(E - E^0 \right) / RT \right] + K_3 a_{\mathrm{H^+}} \exp\left[-F \left(E - E^0 \right) / RT \right]} \tag{30}$$

with Eq. (22).

For the *rds* we write

$$v_{q+1} = \Gamma k_{q+1} \theta_q \tag{31}$$

which then becomes

$$v_{\mathrm{q+1}} = \frac{\Gamma k_{\mathrm{q+1}}^0 \exp\left[\left(1 - \alpha_{\mathrm{q+1}} \right) n_{\mathrm{q+1}} F \left(E - E^0 \right) / RT \right]}{1 + \prod_{j=1}^{q} K_j' + \sum_{i=1}^{q-1} \prod_{j=i+1}^{q} K_j'} \tag{32}$$

where we have also used Eq. (18).

If both the second and last terms in the denominator of Eq. (32) are small compared to one, Eq. (32) predicts the reaction order Ω_{H^+} to be zero and the Tafel slope to be $\ln(10)\,RT/\left[\left(1-\alpha_{q+1}\right)n_{q+1}\right]F$, corresponding to 120 mV for $\alpha_{q+1} = 0.5$ and $n_{q+1} = 1$. If the second term in the denominator is dominating the reaction order is given by $\Omega_{H^+} = \sum_{j=1}^{q} p_j$ and the Tafel slope by $\ln(10)RT/\left[\sum_{j=1}^{q} n_j + \left(1-\alpha_q\right)n_q\right]F$. A similar relation applies to each of the products $\prod_{j=i+1}^{q} K'_j$ in the last sum in the denominator. This therefore leads to a simple counting procedure for establishing possible reaction orders and corresponding Tafel slopes for a given path in **Scheme I**.

Examples of the application of Eq. (32) to various cases are given in Table 1. Expressions similar to some of those in Table 1 have been previously formulated by Bockris and others [12, 34, 35, 36, 37] for an alkaline context.

The first entry of Table 1,

$$i_{CC} = 4Fv_{CC} \approx \frac{4F\Gamma k_2^0 \exp\left[(1-\alpha_2)\,F(E-E^0)/RT\right]}{1 + K_1 a_{H^+} \exp\left[-F(E-E^0)/RT\right]} \tag{33}$$

will be of particular importance below. Eq. (33) predicts a Tafel slope of 40 mV at low potential and 120 mV at high if $\alpha_2 = 0.5$,

$$i_{CC} \approx 4F\Gamma k_2^0 K_1^{-1} a_{H^+}^{-1} \exp\left[(2-\alpha_2)\,F(E-E^0)/RT\right];\ K_1 a_{H^+} \exp\left[\frac{-F}{RT}(E-E^0)\right] >> 1 \tag{34}$$

$$i_{CC} \approx 4F\Gamma k_2^0 \exp\left[(1-\alpha_2)\,F(E-E^0)/RT\right];\ K_1 a_{H^+} \exp\left[\frac{-F}{RT}(E-E^0)\right] << 1 \tag{35}$$

It also predicts that the potential of the transition between these limiting Tafel slopes will decrease with decreasing pH.

Under certain conditions the Tafel slope and the reaction order may be related through Equations (28) and (32). Since the current is proportional to θ_q and k_{q+1}, Eq. (31), and k_{q+1} is independent of a_{H^+}, we obtain with Eq. (28)

$$\Omega_{ox,\,H^+} = \left(\frac{\partial \log \theta_q}{\partial \log a_{H^+}}\right)_{E,T} = \left(\frac{a_{H^+}}{\theta_q}\right)\left(\frac{\partial \theta_q}{\partial a_{H^+}}\right)_{E,T} = -\frac{\left(\sum_{j=1}^{q} p_j\right)\left(\prod_{j=1}^{q} K'_j\right) + \sum_{i=1}^{q-1}\left[\left(\sum_{j=i+1}^{q} p_j\right)\left(\prod_{j=i+1}^{q} K'_j\right)\right]}{1 + \prod_{j=1}^{q} K'_j + \sum_{i=1}^{q-1}\prod_{j=i+1}^{q} K'_j} \tag{36}$$

where we have used that $a_{H^+}\partial K'_i/\partial a_{H^+} = p_i K'_i$.

The Tafel slope is given through

$$(b')^{-1} = \left(\frac{\partial \log i}{\partial E}\right)_{a_{H^+},T} = \left(\frac{\partial \log k_{q+1}}{\partial E}\right)_{a_{H^+},T} + \left(\frac{\partial \log \theta_q}{\partial E}\right)_{a_{H^+},T} = \frac{\left(1-\alpha_{q+1}\right)n_{q+1}F}{\ln(10)\,RT} + \frac{1}{\ln(10)\,\theta_q}\left(\frac{\partial \theta_q}{\partial E}\right)_{a_{H^+},T} \tag{37}$$

where we have used Eqs. (31) and (18). Using Eq. (28) in Eq. (37) gives

$$(b')^{-1} = \left(\frac{\partial \log i}{\partial E}\right)_{a_{H^+},T} = \frac{\left(1-\alpha_{q+1}\right)n_{q+1}F}{\ln(10)\,RT} + \frac{F}{\ln(10)\,RT}\frac{\left(\sum_{j=1}^{q} n_j\right)\left(\prod_{j=1}^{q} K'_j\right) + \sum_{i=1}^{q-1}\left[\left(\sum_{j=i+1}^{q} n_j\right)\left(\prod_{j=i+1}^{q} K'_j\right)\right]}{1 + \prod_{j=1}^{q} K'_j + \sum_{i=1}^{q-1}\prod_{j=i+1}^{q} K'_j} \tag{38}$$

where we have also used that $\partial K'_i/\partial E = -\left(n_i F/RT\right)K'_i$ from Eq. (22).

If the sum over p_j in the first term of the numerator of Eq. (36) is equal to the sum over n_j in the first term of the numerator of Eq. (38) and the sum over p_j in the second term of the numerator of Eq. (36) is equal to the sum over n_j in the second term of the numerator of Eq. (38), Eq. (38) reduces to

$$(b')^{-1} = \frac{F}{\ln(10)\,RT}\left[\left(1-\alpha_{q+1}\right)n_{q+1} - \Omega_{ox,\,H^+}\right] \tag{39}$$

where b' is defined through the base-10 logarithm, $b' = (\partial E/\partial \log i)_{a_{H^+},T}$. The conditions listed above for Eq. (39) to be fulfilled are trivially valid for the C, CC, CCC, and CCCC mechanisms. They are also fulfilled for any approximation to other mechanisms that would meet these criteria. Eq. (39) corresponds to Eq. (14b) in Ref. [38]. Following a

derivation similar to that in Ref. [38], Equations (21) and (31) can easily be shown to result in Eq. (39) for the CC mechanism even in the presence of adsorbate-adsorbate interactions (Frumkin isotherm).

It was recently shown that derivations based on the assumption of quasi-equilibrium in all but the rate-determining step may not capture all the different Tafel slopes that would emerge from full kinetic models in the steady-state approximations [39]. Such models were therefore not advised to be used in the elucidation of the expressions for the current as a function of potential [39]. A derivation of an expression for the electrochemical oxide path, consisting of steps (2) and (3) followed by an associative desorption of oxygen, is given in the Supplementary material. The full expressions are difficult to use in practice, but does reduce to an expression of the same type as Eq. (33) under the conditions specified in the Supplementary material. We conclude there that this equation is valid also under the less restrictive condition of arbitrary relative rates of the two first steps in the CC mechanism.

3.3. A bimolecular mechanism: The oxide path

A description of the oxide path [13] is also included as it will become relevant for the discussion later on. The oxide path can be written

$$\mathrm{H_2O}(\ell) \underset{k_{-1}}{\overset{k_1}{\rightleftharpoons}} \mathrm{OH_{ad}} + \mathrm{H^+(aq)} + \mathrm{e^-} \tag{40}$$

$$2\mathrm{OH_{ad}} \underset{k^0_{-2}}{\overset{k^0_2}{\rightleftharpoons}} \mathrm{O_{ad}} + \mathrm{H_2O}(\ell) \tag{41}$$

$$\mathrm{O_{ad}} \underset{k_{-3}}{\overset{k_3}{\rightleftharpoons}} \frac{1}{2}\mathrm{O_2(g)}, \tag{42}$$

Superscript zero is included for the rate constants for reaction (41) since the rate constants for this reaction step is purely chemical and assumed to be potential independent. The full current expression with reaction (41) as the *rds* can be obtained by following the same procedure as above, which will give

$$i = 2F\Gamma k^0_2\theta_1^2 = \frac{2F\Gamma k^0_2}{\left\{1 + K_1 a_{\mathrm{H^+}} \exp\left[-F\left(E - E^0\right)/RT\right]\right\}^2} \tag{43}$$

Here Eq. (20) has been solved for θ_1 and inserted into the rate equation for reaction (41), in which the rate of the reverse reaction has been neglected. For low potentials the current expression can be approximated to Eq. (44) which gives a Tafel slope of 30 mV dec^{-1},

$$i \approx \frac{2F\Gamma k^0_2}{\left(K_1 a_{\mathrm{H^+}}\right)^2} \exp\left[2F\left(E - E^0\right)/RT\right] \tag{44}$$

For high potentials the Tafel slope will be infinite.

4. Results

4.1. Crystal structure

X-ray diffractograms of all the compositions are shown in Fig. 1(a), all demonstrating the same rutile-type crystal structure. A shift in peak position can be seen with increasing iridium content from the pure ruthenium oxide clearly demonstrated by the reflection located in the range 34-36° in Fig. 1(b). The lattice parameters obtained by Rietveld refinement as function of ruthenium fraction are shown in Fig. 2. The results of Rietveld refinement are summarized in the Supporting material, which in addition to axis lengths also contains crystallite size. A linear contraction of the cell volume is an indication of formation of a solid solution. An almost linear decrease is seen for the c-lattice parameter, with that of Ir60 being somewhat longer than what is expected for a linear contraction. The values and trends are in good agreement with what has been reported for $\mathrm{Ir}_x\mathrm{Ru}_{1-x}\mathrm{O}_2$ powders produced by hydrolysis synthesis previously [10]. Owe et al. [10] found a deviation from linear contraction for samples with X_{Ir}=0.75, which were a mix of pure iridium oxide and an Ir-Ru solid solution phases. The deviation from linear contraction for Ir60 could therefore indicate that some pure iridium oxide is present in this sample.

Mechanism	Rate v, kinetic model
CC	$\frac{\Gamma k_2^0 \exp\left[(1-\alpha_2)F(E-E^0)/RT\right]}{1+K_1 a_{H^+} \exp\left[-F(E-E^0)/RT\right]}$
CCC	$\frac{\Gamma k_3^0 \exp\left[(1-\alpha_3)F(E-E^0)/RT\right]}{1+K_2K_1 a_{H^+}^2 \exp\left[-2F(E-E^0)/RT\right]+K_2 a_{H^+} \exp\left[-F(E-E^0)/RT\right]}$
CCCC	$\frac{\Gamma k_4^0 \exp\left[(1-\alpha_4)F\left(E-E^0\right)/RT\right]}{1+K_1K_2K_3 a_{H^+}^3 \exp\left[-3F\left(E-E^0\right)/RT\right]+K_2K_3 a_{H^+}^2 \exp\left[-2F\left(E-E^0\right)/RT\right]+K_3 a_{H^+} \exp\left[-F\left(E-E^0\right)/RT\right]}$
EP	$\frac{\Gamma k_2}{1+K_1 \exp\left[-F(E-E^0)/RT\right]}$
PC, PE	$\frac{\Gamma k_2^0 \exp\left[(1-\alpha_2)F(E-E^0)/RT\right]}{1+K_1 a_{H^+}}$
CP	$\frac{\Gamma k_2}{1+K_1 a_{H^+} \exp\left[-F(E-E^0)/RT\right]}$
EC	$\frac{\Gamma k_2^0 \exp\left[(1-\alpha_2)F(E-E^0)/RT\right]}{1+K_1 \exp\left[-F(E-E^0)/RT\right]}$
CE	$\frac{\Gamma k_2^0 \exp\left[(1-\alpha_2)F(E-E^0)/RT\right]}{1+K_1 a_{H^+} \exp\left[-F(E-E^0)/RT\right]}$
PEC, PEE	$\frac{\Gamma k_3^0 \exp\left[(1-\alpha_3)F(E-E^0)/RT\right]}{1+K_1K_2 a_{H^+} \exp\left[-F(E-E^0)/RT\right]+K_2 \exp\left[-F(E-E^0)/RT\right]}$
EPC, EPE	$\frac{\Gamma k_3^0 \exp\left[(1-\alpha_3)F(E-E^0)/RT\right]}{1+K_1K_2 a_{H^+} \exp\left[-F(E-E^0)/RT\right]+K_2 a_{H^+}}$
ECP	$\frac{\Gamma k_3}{1+K_1K_2 a_{H^+} \exp\left[-2F(E-E^0)/RT\right]+K_2 a_{H^+} \exp\left[-F(E-E^0)/RT\right]}$
CEP	$\frac{\Gamma k_3}{1+K_1K_2 a_{H^+} \exp\left[-2F(E-E^0)/RT\right]+K_2 \exp\left[-F(E-E^0)/RT\right]}$
CPE	$\frac{\Gamma k_3^0 \exp\left[(1-\alpha_3)F(E-E^0)/RT\right]}{1+K_1K_2 a_{H^+}^2 \exp\left[-F(E-E^0)/RT\right]+K_2 a_{H^+}}$
PCE	$\frac{\Gamma k_3^0 \exp\left[(1-\alpha_3)F\left(E-E^0\right)/RT\right]}{1+K_1K_2 a_{H^+}^2 \exp\left[-F\left(E-E^0\right)/RT\right]+K_2 a_{H^+} \exp\left[-F\left(E-E^0\right)/RT\right]}$
PEPE	$\frac{\Gamma k_4^0 \exp\left[(1-\alpha_4)F\left(E-E^0\right)/RT\right]}{1+K_1K_2K_3 a_{H^+}^2 \exp\left[-F\left(E-E^0\right)/RT\right]+K_3K_2 a_{H^+} \exp\left[-F\left(E-E^0\right)/RT\right]+K_3 a_{H^+}}$
EPPE	$\frac{\Gamma k_4^0 \exp\left[(1-\alpha_4)F\left(E-E^0\right)/RT\right]}{1+K_1K_2K_3 a_{H^+}^2 \exp\left[-F\left(E-E^0\right)/RT\right]+K_3K_2 a_{H^+}^2+K_3 a_{H^+}}$

Table 1: Pathways involving coupled and decoupled proton-electron reaction steps, Eq. (32). The constants K_i are ratios of reverse and forward rate constants as in the balance of the text, numbered consecutively along the path.

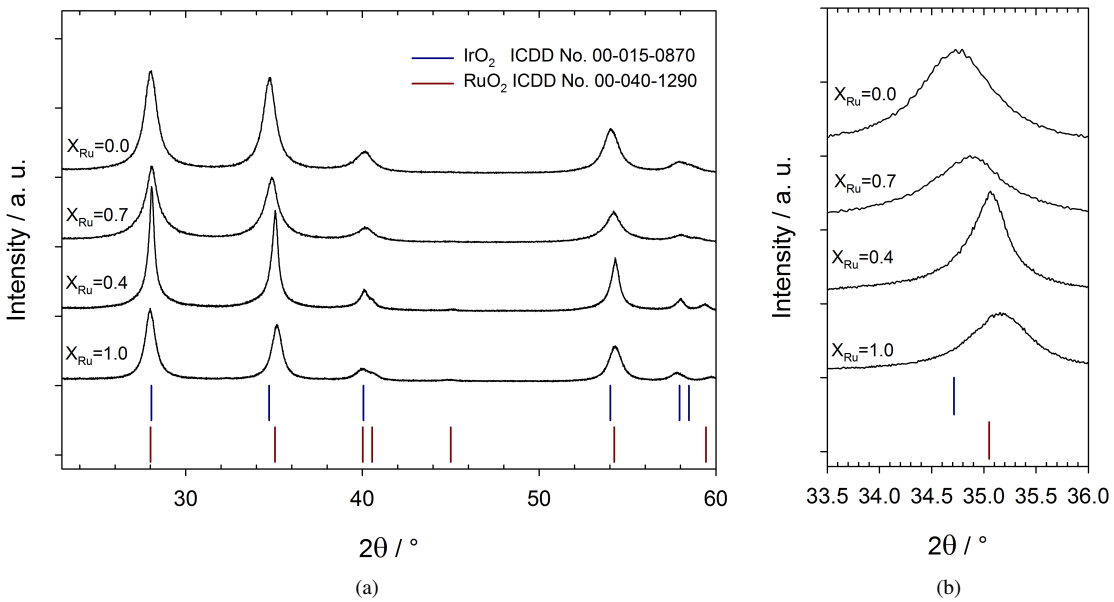

Figure 1: (a) One X-ray diffractogram of all compositions, (b) zoom-in on (101) reflection located at 2θ ~34-35 °.

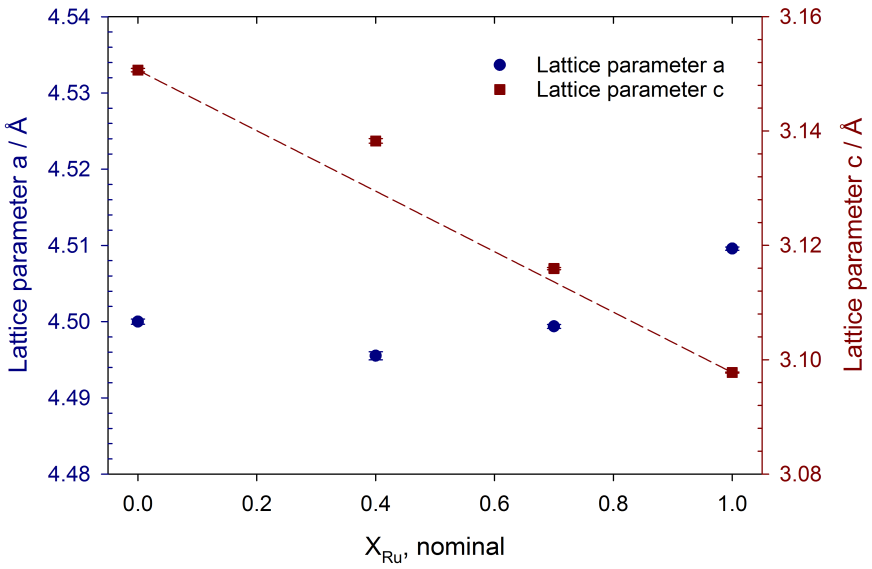

Figure 2: Lattice parameters a and c obtained by Rietveld refinement of the X-ray diffractograms presented as a function of ruthenium fraction.

Attempts of including strain in the Rietveld refinements did not yield any significant improvements in the fits, and were left out of the analysis. However, the effects of strain on catalytic activity do not appear to be very important in oxides [40], as opposed to metals [41].

4.2. Electrochemical characterization

Voltammograms obtained at electrodes of all compositions recorded with 50 mV s^{-1} in $HClO_4$ pH 0 are shown in Fig. 3. The pure IrO_2 shows a broad anodic wave starting at approximate 0.6 V and possibly consisting of several peaks. It is perhaps possible to distinguish three peaks located at 0.8 V, 1.0 V and 1.15 V, although these are not well defined. Three anodic peaks can be distinguished for the mixed oxides and the ruthenium oxide. The first is located at approximately 0.55 V for all three. The second is, however, not located at the same potential for all; for both RuO_2 and Ir60 it is located close to 0.8 V, but for Ir30 it has been shifted to a more anodic potential and is present at 0.95 V. The third anodic peak is located close to 1.2 V, maybe higher for RuO_2. This peak overlaps with the onset of oxygen evolution, however, and it is thus difficult to define the precise peak location. The voltammograms in Fig. 3 are quite

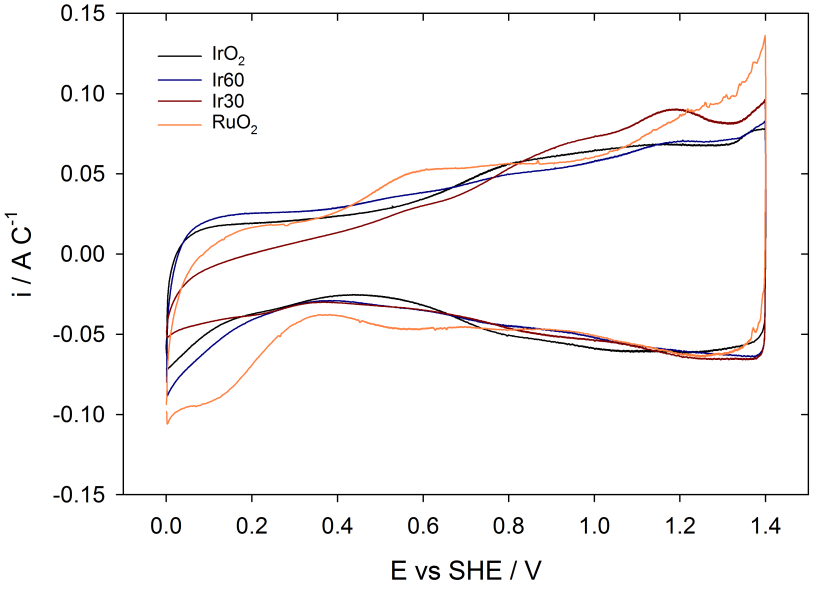

Figure 3: CV of all compositions recorded with sweep rate 50 mV s^{-1} in $HClO_4$ pH 0. E is the potential and i the current.

similar to those of solid solutions and also to physical mixtures of IrO_2 and RuO_2 in the same ratios as reported by Owe *et al.* [10], indicating that the response is to some extent simply an overlap of the voltammograms of the end members.

The polarization curves obtained for all compositions are shown in Fig. 4. (The data shown were compensated for 85% of the ohmic resistance at 1.35 V as explained in Section 2.) As expected an increasing activity is found as function of ruthenium fraction. These set of data show quite different behavior in the potential window employed. A lower potential region with developed Tafel behavior is seen for all compositions. However, this region is not equally extensive for all. The transition to a steeper slope at high potential is seen for all compositions, but occurs at a much lower potential for RuO_2 than for IrO_2. The mixed oxides demonstrate both the lower region and the transitioning into a regime with steeper Tafel slope, but they have a less defined transition than what is seen for RuO_2.

We have previously established the presence of some surface segregation for samples of $Ir_{0.75}Ru_{0.25}$ (83 mol% surface concentration of Ir), $Ir_{0.5}Ru_{0.5}$ (88 mol% surface concentration of Ir) and $Ir_{0.25}Ru_{0.75}$ (67 mol% surface concentration of Ir) [10] synthesized by the hydrolysis method. These numbers may be taken as indications of the degree of surface segregation in the Ir30 and Ir60 samples also in this work. Assuming that the polarization curves represent a linear superposition of contributions from ruthenium and iridium oxide, in accordance with the voltammograms

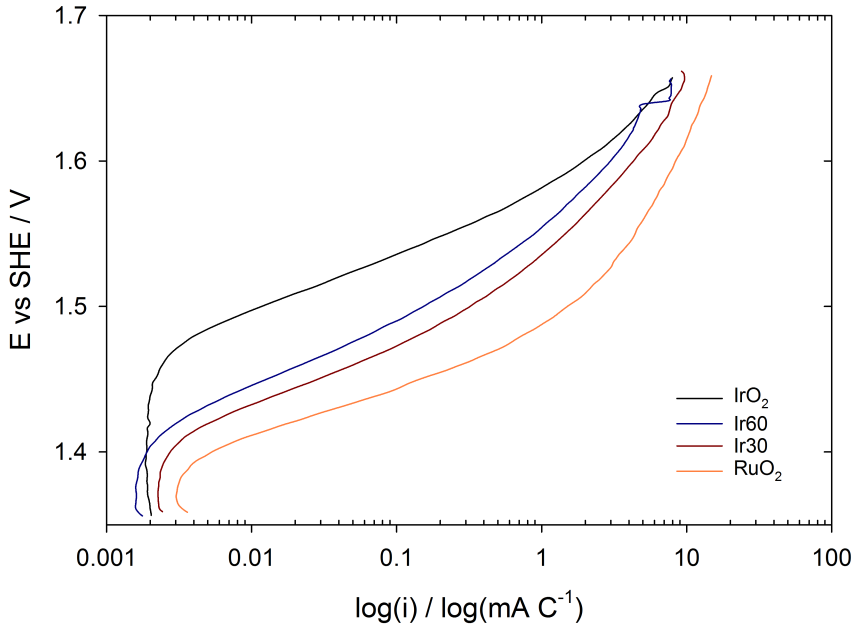

Figure 4: Polarization curves of all composition recorded at pH 0.

in Fig. 3 and Reference [10], the polarization curves in Fig. 4 are in accordance with a similar degree of surface segregation also here.

In Fig. 5 Tafel plots of all compositions as function of pH are presented. An onset at lower potential for the transition into the potential region of higher Tafel slope is seen with increasing pH as well as with increasing ruthenium fraction for all samples. A convergence of the polarization curves in the high potential region is seen, which is consistent with the pH-independence expected after transition from the region best described by Eq. (34) to the region described by Eq. (35), as the latter does not depend on the proton activity.

4.3. Polarization curve fitting

All curves were fitted according to Eq. (1) and to Eq. (33). (As will be discussed below, we note that Eq. (33) may be approximated by limiting forms of the expressions for the mononuclear path.) The result of both fits are shown in Fig. 6 for IrO_2 pH 0, 1, 2 and 3. Fits to Eq. (1) thus included an ohmic drop term in addition to that compensated for by the potentiostat (Section 2), iR_Ω in Eq. (1), which allows for extension of the linear region. Previously the upwards bending was interpreted as being caused by a constant resistance due to evolution of oxygen gas [10, 24, 25]. However, in view of the fact that we in this work found the transition point to vary systematically with pH and composition rather than appearing at the same current we interpret this feature as the development of a second Tafel slope as derived in the models above. Thus, fits obtained when the full current expression is used, Eq. (33), describe the polarization curves of iridium well, Fig. 6, and are taken as representative for the reaction mechanism itself although it does show some minor deviation in some areas.

For IrO_2 pH 0 to 2, Figures 6(a) through (c), slightly steeper Tafel slopes result from the fit compared to what can be seen by visual inspection of the experimental curve in the low potential region. In the final potential range the curve based on the model is straightened out more than the experimental curve for all measurements. Included in these figures are three horizontal dashed lines which divide the curves into four different segments. These lines represent the potentials where the second term in the denominator in Eq. (33), $K_1 a_{H^+} \exp\left[-F(E-E^0)/RT\right]$, is calculated equal to 0.1, 1, and 10. The potential at which this expression is equal to 1 will indicate the transition potential, E_T, between the higher and lower Tafel behavior, and 10 and 0.1 where the contribution of this term in the denominator is 90 and

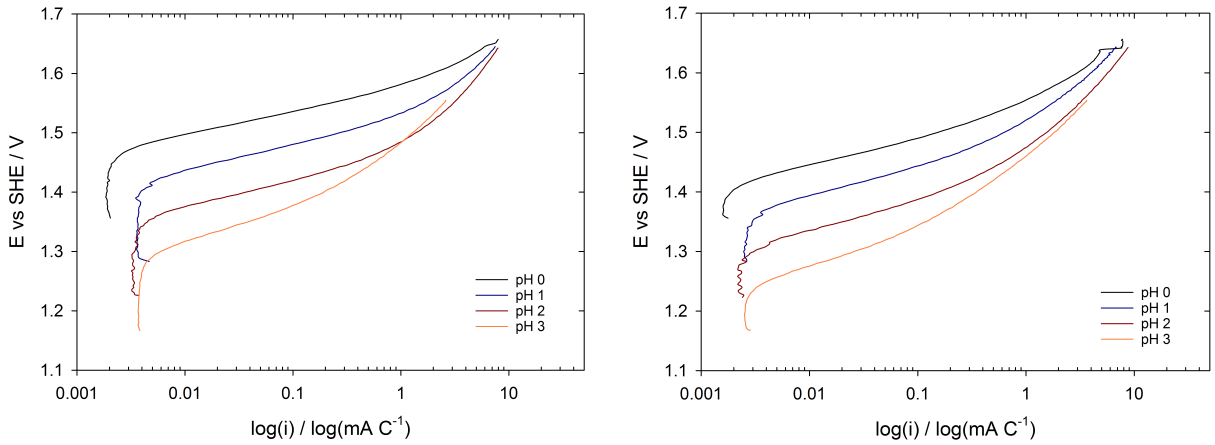

Figure 5: Polarization curves of (a) IrO_2, (b) Ir60, (c) Ir30 and (d) RuO_2 as function of pH.

10%, respectively. The current behavior should therefore best be approximated to Eq. (34) at low potentials (area I) and, in the absence of complications due to gas blockage or degradation, by Eq. (35) at high potentials (area IV).

As is seen in Fig. 6(b) and 6(c) the fitted polarization curve describes both the high and low potential region and the transition in between them quite well. The polarization curve recorded for pH 0, Fig. 6(a), does not extend far into the high potential region. At pH 3 on the other hand, a well-developed lower potential region is not seen prior to the onset of the transition. In this case the fit demonstrates a slightly less steep Tafel slope than the experimental curve suggests. However, since this region is limited, an attempt of finding a linear region here graphically could result in an erroneous slope and description of the curve.

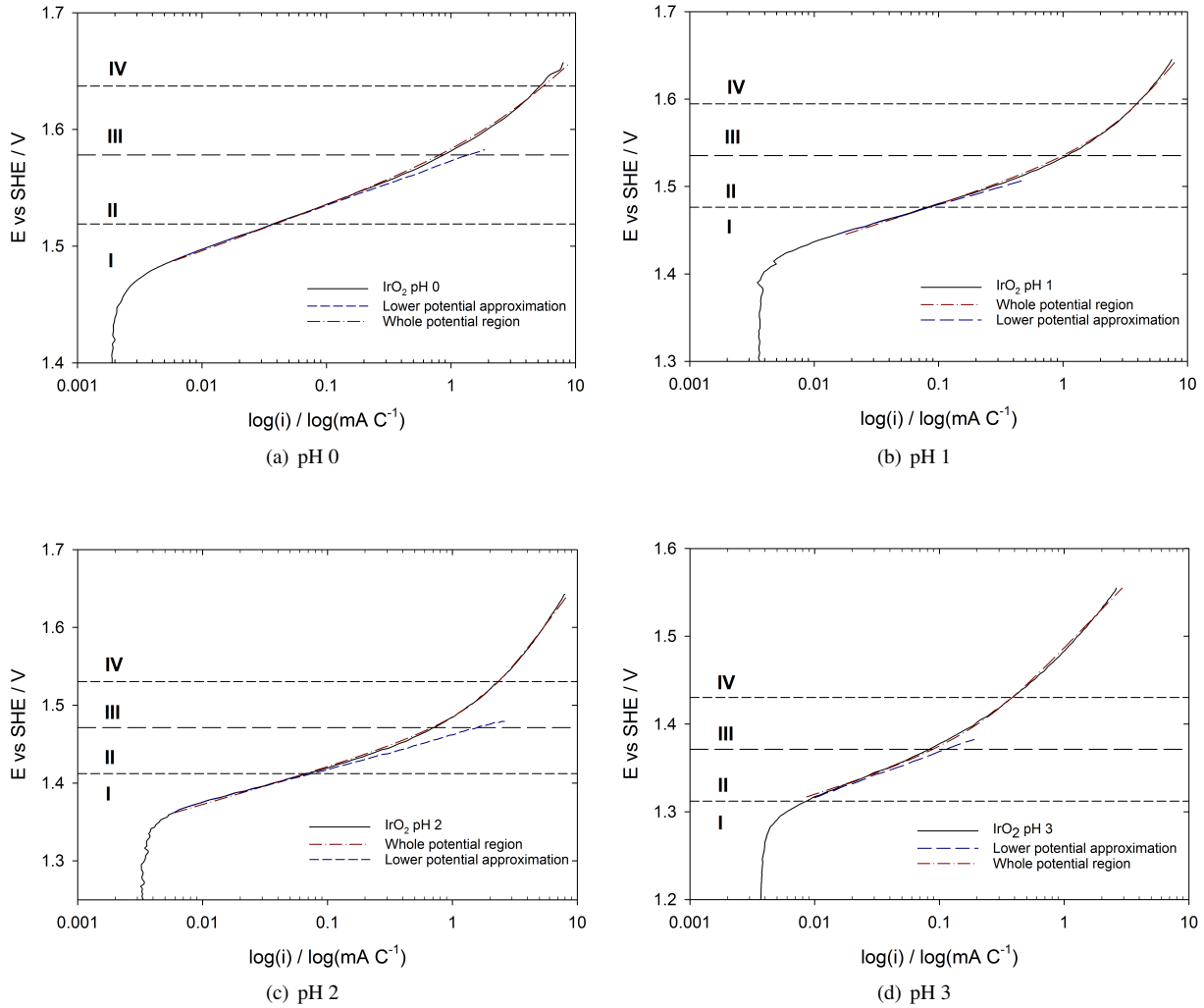

(a) pH 0 (b) pH 1

(c) pH 2 (d) pH 3

Figure 6: Fitted polarization curves of IrO_2 recorded in $HClO_4$ pH (a) 0, (b) 1, (c) 2 and (d) 3.

Curve fits for the other compositions as function of pH followed the trends described for the pure iridium oxide. Values obtained from these fits are reported in Table 2 together with the parameters obtained for the other compositions. However, well-described lower and higher potential regions could not be obtained simultaneously for the pure ruthenium oxide recorded in pH 0, 1 and 2. This is illustrated in Fig. 7(a) for RuO_2 pH 1. The slopes suggested from the fit are too steep for the lower region, not steep enough in the high-potential region, and the transition region is not well fitted either.

The Tafel slope of the low potential region of the oxide path (Eq. (43)) with the reaction in Eq. (41) as the *rds* is 30 mV dec^{-1}. This could be suggested as a better description for the RuO_2 pH 0, 1 and 2 since it was difficult to obtain good fits in both the lower and higher potential region at the same time. These polarization curves were therefore also fitted to Eq. (43). Better fits were, however, not obtained. An example is shown for RuO_2 at pH 1 in Fig. 7(b). The fit is substantially inferior to that obtained with the CC path (Eq. (33)).

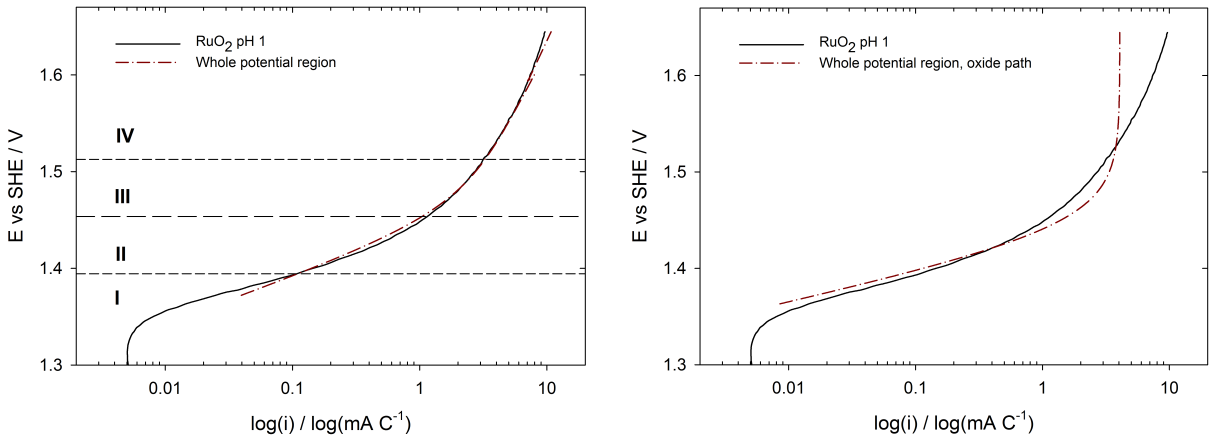

Figure 7: Fit of RuO_2 at pH 1, modeled with (a) the CC path, Eq. (33), and (b) the oxide path. Eq. (43).

Table 2: Summary of fitted parameters for all compositions recorded in the pH range 0 through 3 in $HClO_4$. The lower region Tafel slopes in mV dec^{-1}, the intercept with the y-axis and the product of rate constant with activity of protons are reported. The quantity $K_1 a_{H+} \exp\left[FE^0/RT\right]$ is defined through Eq. (33). E_{Low} is the potential boundary between area I and II, E_{High} between III and IV and E_T is the transition potential between the two Tafel regions, and is the boundary between area II and III.

X_{Ru}	pH	a_l	b_l	$K_1 a_{H+} \exp\left[FE^0/RT\right]$	E_{Low}	E_T	E_{High}
		V	mV dec^{-1}		V	V	V
IrO_2	0	1.570	37.5	4.91E+26	1.519	1.578	1.637
	1	1.522	44.3	9.29E+25	1.476	1.535	1.595
	2	1.465	46.5	7.67E+24	1.412	1.471	1.530
	3	1.402	42.2	1.55E+23	1.312	1.371	1.430
Ir60	0	1.527	41.2	5.76E+25	1.464	1.523	1.582
	1	1.479	42.6	6.57E+24	1.408	1.467	1.527
	2	1.424	44.2	6.74E+23	1.350	1.409	1.468
	3	1.356	41.8	1.44E+22	1.251	1.310	1.369
Ir30	0	1.513	41.6	3.93E+25	1.454	1.513	1.572
	1	1.464	43.3	4.72E+24	1.400	1.459	1.518
	2	1.407	42.4	2.95E+23	1.329	1.388	1.447
	3	1.346	42.2	1.39E+22	1.250	1.309	1.368
RuO_2	0	1.488	45.4	3.49E+25	1.451	1.510	1.569
	1	1.438	47.8	3.83E+24	1.394	1.454	1.513
	2	1.379	46.9	2.43E+23	1.324	1.383	1.442
	3	1.323	45.0	1.42E+22	1.251	1.310	1.369

The Tafel slopes for the low potential region found from fitting simultaneously the entire potential region are shown as function of pH in Fig. 8(a). The values are in the range of 37.5 through 48.0 mV dec^{-1}, displaying no unique trend with pH in accordance with Eq. (34). The Tafel slopes for RuO_2 and the mixed oxides are independent of pH, whereas IrO_2 goes through a maximum for pH 2. There is no correlation between the lower Tafel slope at pH

0 for IrO_2 and the reaction order, Eq. (39). This and the fact that the electrode was rotated at 1800 rpm during the measurements make it unlikely that the maximum in the Tafel slope is associated with any lack of buffering capacity at the highest pH. The slopes of the mixed oxides are close in value, and RuO_2 demonstrates the largest values.

In Fig. 8(b) the logarithm of the product $K_1 a_{H+} \exp\left[FE^0/RT\right]$ has been plotted as function of pH. All compositions demonstrate a close to linear decrease with a slope approximately in the range range from -1.2 to -1.1. This is expected if the model describing the current behavior in the full potential range is able to take into consideration the pH variations correctly and the ratio of the standard rate constants is independent of the proton concentration.

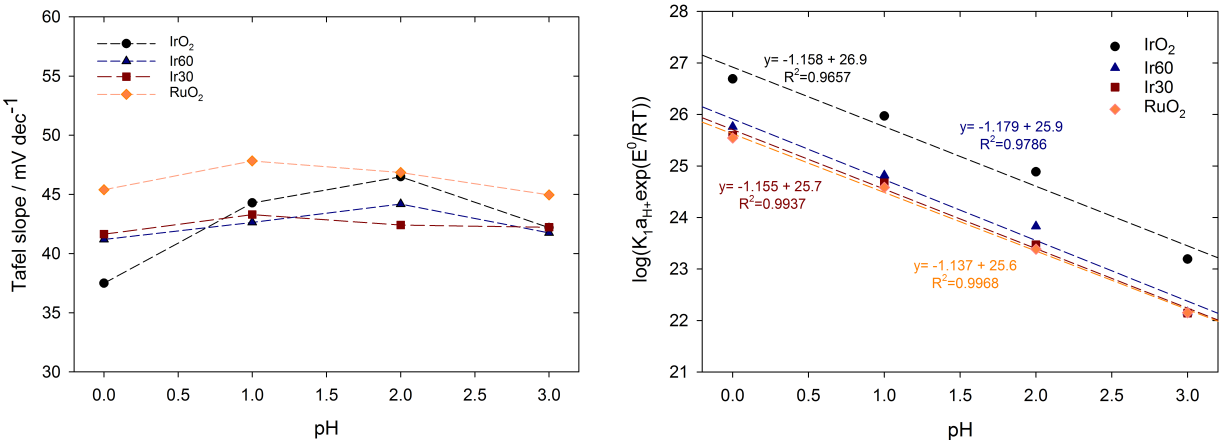

(a) (b)

Figure 8: (a) Low-potential Tafel slopes and (b) product of $K_1 a_{H+} \exp\left[FE^0/RT\right]$ as function of pH from fitting the polarization curves in the whole potential region.

Fig. 9 shows the cyclic voltammograms at 350 mV s^{-1} for IrO_2, Ir60, Ir30, and RuO_2 at pH = 1 before and after recording the polarization curve. The voltammograms before and after performing the LSV differ only insignificantly for IrO_2 and Ir60. For Ir30 some reduction in voltammetric charge is apparent. For RuO_2 the voltammetric charge is significantly reduced. In all cases the voltammetric features are retained. The relative stability of the compositions at other pH's were similar, but in general stability improved with increasing pH. Implications will be discussed in Section 5.4 below.

4.4. Determination of proton reaction order

Reaction orders are usually evaluated from the slope when the natural logarithm of the current density is plotted as function of the natural logarithm of proton concentration under constant applied potential. The values of constant current density at constant potential was not possible to obtain directly in this work. The regions where Eq. (34) is applicable for the measurements at all pH values were not always accessible and were found in varying potential ranges. Therefore, in order to evaluate the reaction order with respect to protons, these slopes had to be extrapolated.

The resulting plots for all compositions are shown in Fig. 10 evaluated at constant potentials of 1.35, 1.4 and 1.45 V. Table 3 summarizes the reaction orders found for all compositions. The reaction order for iridium oxide was found to be -1.5, for ruthenium oxide -1.2, and the mixed oxides demonstrate values in between these extremes. Reaction orders were found to be -1.4 and -1.3 in average for Ir60 and Ir30, respectively. Neither of these catalysts therefore demonstrates the theoretical value of -1 expected for the CC path at low overpotentials.

5. Discussion

5.1. Polarization curve fitting

The CC path gives in general a good description of the polarization curves for the OER displayed by the $Ir_xRu_{1-x}O_2$ catalysts obtained by hydrolysis synthesis. The full current expression, Eq. (33), predicts well both the lower and

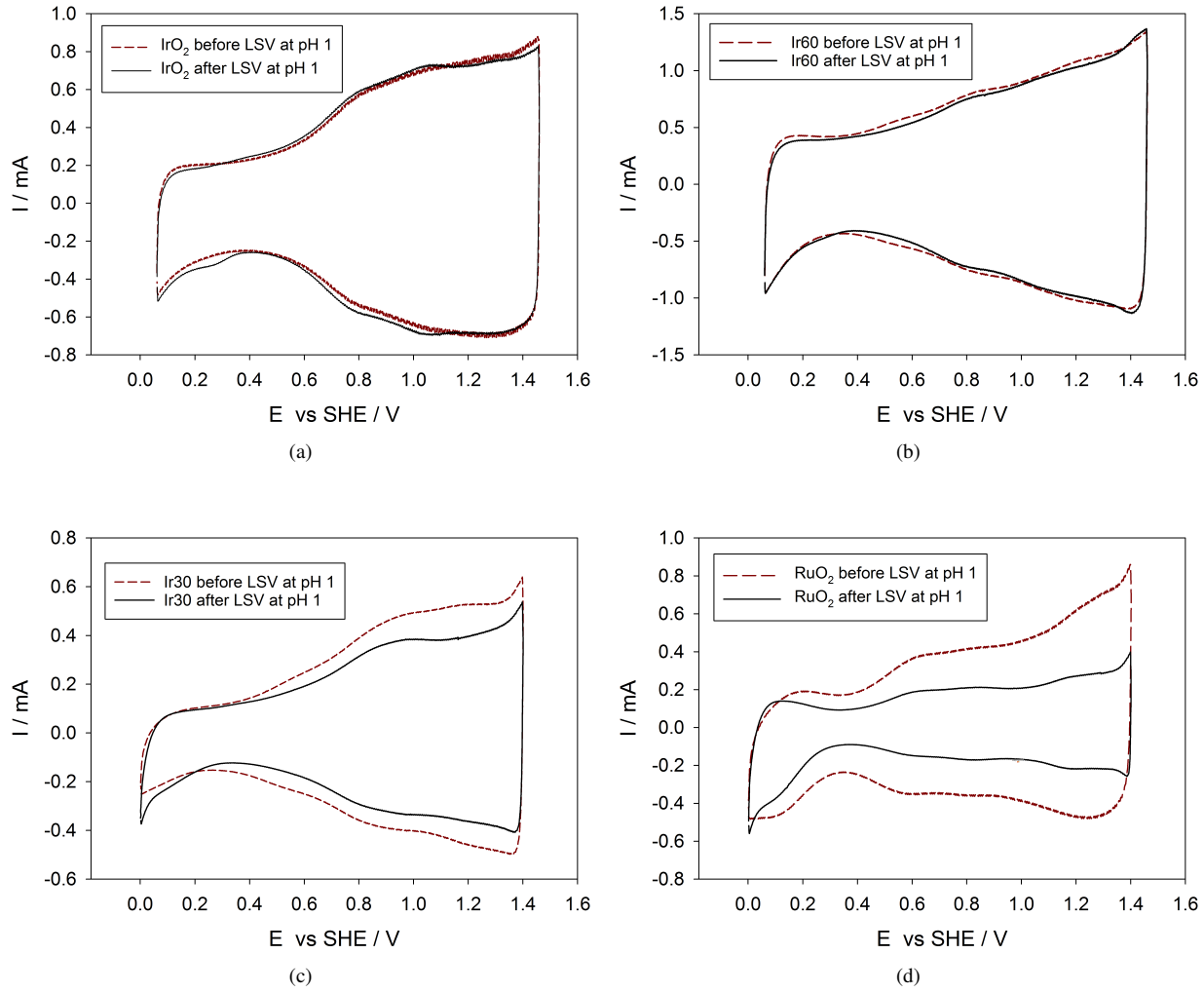

Figure 9: Cyclic voltammograms at 350 mV s^{-1} for (a) IrO_2, (b) Ir60, (c) Ir30, and (d) RuO_2 at pH = 1. The dashed (red) curve shows the CV recorded prior to recording the polarization curve (LSV), and the solid (black) curve the CV recorded after the LSV. The currents shown are raw data, i.e. not normalized with respect to geometric area nor to voltammetric charge.

Table 3: Reaction orders with respect to proton concentration for IrO_2, Ir60. Ir30 and RuO_2.

	IrO_2	**Ir60**	**Ir30**	**RuO_2**
1.45 V	-1.4	-1.4	-1.3	-1.2
1.40 V	-1.5	-1.4	-1.3	-1.2
1.35 V	-1.5	-1.4	-1.3	-1.2

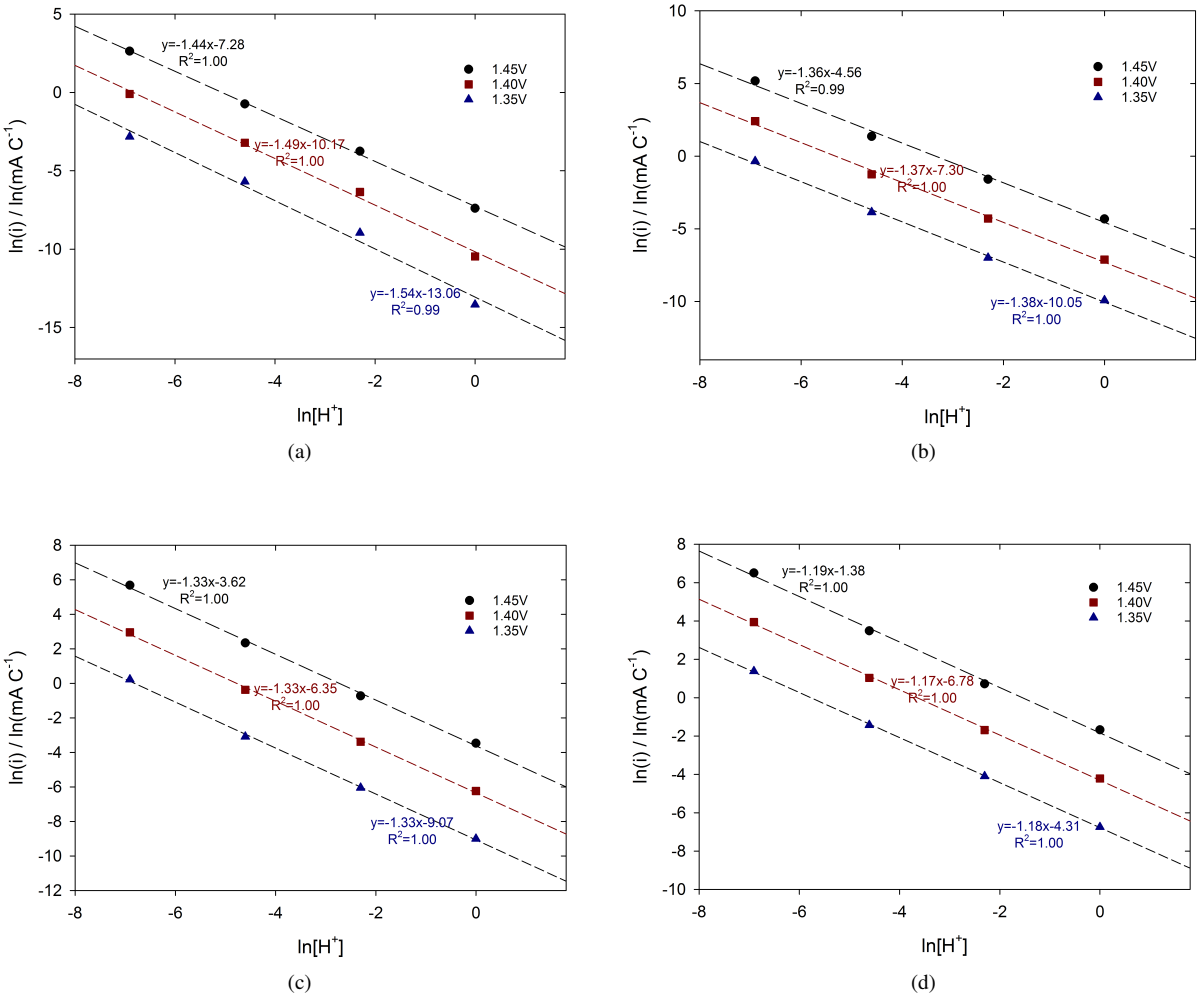

Figure 10: Reaction order plots for (a) IrO_2, (b) Ir60, (c) Ir30 and (d) RuO_2.

higher Tafel slope as well as the transition between them. By visual inspection the model seems to give especially good estimates for the region where the low potential approximation is valid, Eq. (34). The theory predicts decreasing transition potentials and onset to the second Tafel region with increasing pH, and this trend is confirmed by the experimental data. The pH-dependence of the current-voltage relationship is also consistent with the slope of the plot in Fig. 8(b). This plot also indicates that the ratio of rate constants for the oxidation and reduction direction of the first step in the reaction (Eq. (2)), k_1^0 and k_{-1}^0, is independent of pH, in line with the assumptions. Eq. (33) is therefore believed to represent and adequately describe the pH- and current-voltage characteristics of the OER at these samples.

RuO_2 could for some of the pH values not be fitted as well as the other compositions within this model, and these data were not always consistent with a constant symmetry factor. However, fits to models resulting in equations other than those that could be approximated by Eq. (33) led to poorer fits and have to be rejected. In these cases the lower and higher slopes were not in accordance with a constant symmetry factor. As can be seen in Fig. 7 the lower potential region Tafel slope for RuO_2 at pH 1 is evaluated to be too high. The oxide path [13] with reaction of two adsorbed hydroxyl ions to form adsorbed oxygen and water as the *rds* predicts a Tafel slope of 30 mV dec^{-1} in the lower region and an infinite slope at high potentials. With the initial low Tafel slope this model could possibly be a more appropriate description of the RuO_2 recorded at pH 0, 1 and 2. However, the current-voltage relationship emerging from the model for this mechanism is clearly not a good description for these polarization curves, Fig. 7. Eq. (33) therefore appears to be the most appropriate description also for the RuO_2 at all pH values investigated here, even though the fits performed for some polarization curves are not as good as for the other compositions.

The deviations in the fits for RuO_2 pH 0, 1 and 2 are believed to be caused by the instabilities of the catalyst. Deviation from the E-log i behavior predicted by the model in the high potential range is to be expected if a process not included in the model is operative and which causes the experimental current to decrease at higher potentials. Possibilities are blockage of the electrode due to evolved gas or corrosion of the catalyst, both which may cause a reduction of the catalyst surface. However, as is apparent from Fig. 5(d) the current at which the transition to a higher Tafel slope takes place is a function of pH. If gas evolution was the cause for this transition one would expect it to take place at the same oxygen evolution rate, i.e the same current; if the upwards bending of the current at high potential was dominated by gas formation the break point would appear at approximately the same current density. It does not, as can be seen clearly in the potential-log $-i$ plots. Also, the break in the potential-log $-i$ plots appears at roughly the same potential as of Damjanovic *et al.* [13]. A rather illustrating case of this point are the polarization data of Owe *et al.* [27, Fig. 5]. For these the up-turn of the curve is shifted three orders of magnitude from perchloric acid to phosphoric acid of the same concentration, all appearing at approximately the same potential.

Finally, if the too steep slope in the high potential region was caused by gas blocking parts of the electrode, better fits should be obtained by moving the fitting range down in potential. Moving the fitting range to more cathodic potential did not result in better fits, and this could suggest that the Tafel slopes being too high are not due to evolved gas. From these considerations we do therefore not consider gas evolution to be responsible for the apparent higher slope of the E vs. log i curve at high potential nor the poorer fit to the theory.

However, if the current reduction is caused by instabilities of ruthenium at higher potentials this could be accompanied by a reduction of active surface area and thereby a change of charge from the CVs recorded before and after the polarization curves as demonstrated in Fig. 9(c) and 9(d). Evaluation of these and other CVs shows that RuO_2 at pH 0 and 1 suffered the largest decrease of charge over the measurements. For pH 2 and 3 a reduction was also seen, but it was not as significant as for the lower pH values. This is consistent with the current-voltage results for RuO_2 at pH 3 being well described by the suggested model, but less so at lower pH.

The Ir30 samples for all pH value showed a somewhat more moderate decrease of charge, Fig. 9(c), whereas Ir60, Fig. 9(b), and pure iridium oxide, Fig. 9(a), showed a more or less constant charge over the polarization curve measurement. It therefore seems likely that instabilities of ruthenium oxide at higher potentials might be the reason for why the polarization curves of RuO_2, especially at lower pH, are difficult to fit.

The shape of the curves reported in Fig. 4 is similar to previously reported results for similar electrodes [42, 43, 44, 45], which display a low-potential Tafel slope in the same order of magnitude as that found here and frequently a transition to a higher Tafel slope at a potential between 1.5 V and 1.6 V. The low-potential Tafel region in Fig. 4 extends for about two decades for IrO_2 but only slightly more than one decade for RuO_2. This is also similar to previously reported results for iridium-containing oxide layers. For example, Ouattara *et al.* [42], Hu *et al.* [43], Ferro *et al.* [44], Gottesfeld and Srinivasan [45], Marshall and Haverkaamp [46], Mayousse *et al.* [47], Reier *et al.* [48], Stoertzinger *et al.* [49], ten Kortenaar *et al.* [50], Xu *et al.* [51], Yagi *et al.* [52], and De Pauli and Trasatti [53]

all reported polarization curves with a low-potential Tafel region extending over approximately two decades or less, whereas Lyons and Floquet obtained straight Tafel regions over about three orders of magnitude in the current [54]. Damjanovic *et al.* [13] found a low-potential Tafel region of an exceptionally large range, approximately seven orders of magnitude, for Ir electrodes in 1 N $HClO_4$. (Damjanovic *et al.* [13] performed their measurements by reducing the potential from high to low current densities and after anodization at 1 mA cm^{-2} for 20 min. It is therefore likely that their Ir sample represents an iridium oxide.) For these electrodes a rather abrupt change in Tafel slope was observed at ~ 1.5 V vs. SHE, from 120 mV (converted here to the log_{10} base) above to 40 mV below this potential, i.e. at a similar potential as for our IrO_2 case. Although the current scales are not comparable due to the charge normalization employed here, it is from the potential scales clear that the accessible Tafel range is in our case is limited downwards with respect to that of Damjanovic *et al.* [13]. We relate this to a combination of differences in the measurement procedure and surface state. Our measurements were performed at already existing and well defined oxides, and the LSV was conducted from low to high potential. This will make the first part of the LSV part of a voltammogram, albeit at a very low sweep rate, and result in a small current not related to oxygen evolution.

5.2. Proton reaction order

The reaction order based on protons were not estimated to unity as expected for the CC path. On the other hand, fractional orders were obtained in the range of -1.2 to -1.5, and have previously been reported for the OER [55, 44, 56]. Several causes to deviation from unity have been proposed [57]. Fractional reaction orders caused by two competing or parallel pathways of OER occurring simultaneously [57, 58] is one proposed reason. The double layer effect (Frumkin effect) is the one most encountered [56, 59]. The implications of this effect for the current expression is derived in the Supplementary material and gives,

$$\begin{aligned} i_2 &\approx 4F \frac{\Gamma k_2^0 a_{\mathrm{H^+}}^{-(1-\alpha_2)} \exp\left[(1-\alpha_2)\, F(E-E^0)/RT\right]}{1 + K_1 a_{\mathrm{H^+}} \exp\left[-F(E-E^0)/RT\right]} \\ &\sim 4F\Gamma k_2^0 K_1^{-1} a_{\mathrm{H^+}}^{-(2-\alpha_2)} \exp\left[(2-\alpha_2)\, F(E-E^0)/RT\right] \end{aligned} \tag{45}$$

where the last approximation is valid in the low potential region, and will predict a reaction order of -1.5 instead of -1 for α_2 equal to 0.5. This is close to the value found for IrO_2. However, they were found to be higher for the three other compositions. It is interesting to note that the relation in Eq. (39) appears to imply a means of detecting double-layer effects; an apparent reaction order of -1.5 implies a Tafel slope of 30 mV through Eq. (39), whereas Eq. (45) combines an apparent reaction order of -1.5 with a Tafel slope of 40 mV. The latter is in agreement with the experimental results, the former is not.

5.3. Reaction mechanism

As is apparent from the ambiguities disclosed in the theoretical development above the reaction mechanism cannot been uniquely determined by the analysis. The pH- and potential-dependence does limit the number of possible patterns, but the limiting forms of several models are compatible with the experimental results. Marshall and Vaisson-Béthune [39] found that if the assumption of a quasi-equilibrium is avoided kinetic models may give additional Tafel slopes. The electrochemical oxide path, which in terms of its current-voltage characteristics corresponds to the CC path here if the second step of the electrochemical oxide path is *rds*, may thus also give Tafel slopes of 30 mV dec^{-1} and 60 mV dec^{-1}. However, in these cases the high-potential slope is infinite [39, Fig. 2]. As shown in Fig. 7(b) this is not consistent with the experimental results obtained in this study. We therefore conclude that no combinations of composition and pH in this study fall into this category, and that there is an *rds* involved in the reaction mechanism. The existence of an *rds* is also consistent with the theoretical calculations of Rossmeisl *et al.* [6]. We therefore base our analysis on this assumption.

In order to distinguish between the various possible concerted mechanisms compatible with the results quantitative information about the rate constant ratios K_1, K_2, and K_3 in the second (CCC) and third (CCCC) entries in Table 1,

i.e.

$$i \approx 4F\Gamma k_3^0 \exp\left[(1-\alpha_3)F(E-E^0)/RT\right] \times \left\{\frac{1}{1 + K_2 a_{H^+} \exp\left[-F(E-E^0)/RT\right] + K_2 K_1 a_{H^+}^2 \exp\left[-2F(E-E^0)/RT\right]}\right\} \quad (46)$$

and

$$i \approx 4F\Gamma k_4^0 \exp\left[(1-\alpha_4)\, F\left(E-E^0\right)/RT\right] \times \left\{1 + K_1 K_2 K_3 a_{H^+}^3 \exp\left[-3F\left(E-E^0\right)/RT\right] + K_2 K_3 a_{H^+}^2 \exp\left[-2F\left(E-E^0\right)/RT\right] + K_3 a_{H^+} \exp\left[-F\left(E-E^0\right)/RT\right]\right\}^{-1} \quad (47)$$

is required. These can be related to the equilibrium constant and thus the free energy for each of the steps in the reaction mechanism through the free energy-relations in Ref. [6, Equations (11), (12), and (13)]. With these we get

$$K_1 = \exp\left\{\left(0.61\Delta E_O - 0.55\ \text{eV} - eE^0\right) / \left(6.242 \times 10^{18}\ \text{eV J}^{-1} \times kT\right)\right\} \quad (48)$$

$$K_2 = \exp\left\{\left(0.39\Delta E_O + 0.60\ \text{eV} - eE^0\right) / \left(6.242 \times 10^{18}\ \text{eV J}^{-1} \times kT\right)\right\} \quad (49)$$

$$K_3 = \exp\left\{\left(-0.36\Delta E_O + 2.38\ \text{eV} - eE^0\right) / \left(6.242 \times 10^{18}\ \text{eV J}^{-1} \times kT\right)\right\} \quad (50)$$

where ΔE_O is the binding energy for oxygen at the oxide, k the Boltzmann constant, and e the elementary charge. We thus obtain the values $K_1 = 10^{-13}$, $K_2 = 2$, and $K_3 = 2\times10^9$ for iridium oxide ($\Delta E_0 = 1.66$ eV [6]), whereas the values are $K_1 = 2\times10^{-3}$, $K_2 = 8\times10^6$, and $K_3 = 2\times10^3$ for ruthenium oxide ($\Delta E_0 = 2.66$ eV [6]). (In Equations (48) through (50) we have assumed the relation $\Delta G_i = -RT \ln 1/K_i$ ($i = 1, 2, 3$), observing that the rate-constant ratios and hence equilibrium constants correspond to the opposite direction of the reactions as those in Ref. [6], and $E^0 = 1.23$ V.)

With these values we obtain theoretical values for $K_1 a_{H^+} \exp\left(FE^0/RT\right)$ many orders of magnitude too low compared with the experimental results for both RuO_2 and IrO_2 if reaction (3) is *rds*. This indicates that Eq. (33) represents a limiting case for an *rds* which is downstream of the second step, reaction (3) (**Scheme I**). We therefore investigate whether the mononuclear mechanism with step (4) or (5) as *rds* may provide some degree of consistence with the DFT calculations.

Polarization curves based on these values and Equations (46) and (47) are simulated in Fig. 11, for which we also used a charge-transfer coefficient equal to 0.5. Except for the curve for IrO_2 assuming a CCC mechanism, i.e. the *rds* being that of Eq. (4) [6], the curves predict a transition region above 1.4 V. The assumptions that best fit the experimental results is a CCC mechanism for RuO_2 (Eq. (4) being the *rds*) and a CCCC mechanism for IrO_2, i.e. the *rds* being Eq. (5) [6]. These are the only combinations that give reasonable Tafel slopes and reaction orders as well as a reasonable prediction of the transition region. Thus, for RuO_2 $K_2K_3 >> K_1K_2K_3 >> K_3$. If reaction (5) is *rds* this would result in a Tafel slope of 24 mV dec^{-1} and a reaction order $\Omega_{H^+} = -2$ through Eq. (47). However, for RuO_2 $K_2 >> K_1K_2$. If reaction(4) is *rds* this would result in a Tafel slope of 40 mV dec^{-1} and a reaction order $\Omega_{H^+} = -1$ through Eq. (46), consistent with the experimental results. For IrO_2 $K_2K_3 \sim K_3 >> K_1K_2K_3$. If reaction (5) is *rds* this results in a Tafel slope of 40 mV dec^{-1} (Fig. 11) and a reaction order $\Omega_{H^+} = -1$ through Eq. (47). For IrO_2 $K_2 >> K_1K_2$, which would lead to the same Tafel slope and reaction order if reaction (4) is *rds*. However, this *rds* appears to be associated with a transition region that is too low, Fig. 11, which may indicate that the *rds* is reaction (5). This is slightly at odds with conclusion in Rossmeisl *et al.* [6] who found that steps (3) and (4) are rate-determining for RuO_2 and IrO_2, respectively. However, strictly speaking these DFT calculations predict the potential-determining step, i.e. the step that dictates the onset potential for the reaction, rather than the rate-determining step. Also, the results in Ref. [6] were generated for one crystal facet, whereas the catalysts investigated here represent an average over many, also including edges and defects.

Similar calculations based on Eq. (33) and with the equilibrium constants calculated from Equations (48) through (50) did not display the low-potential Tafel slope at all in the relevant potential range. Thus, in order to be consistent with

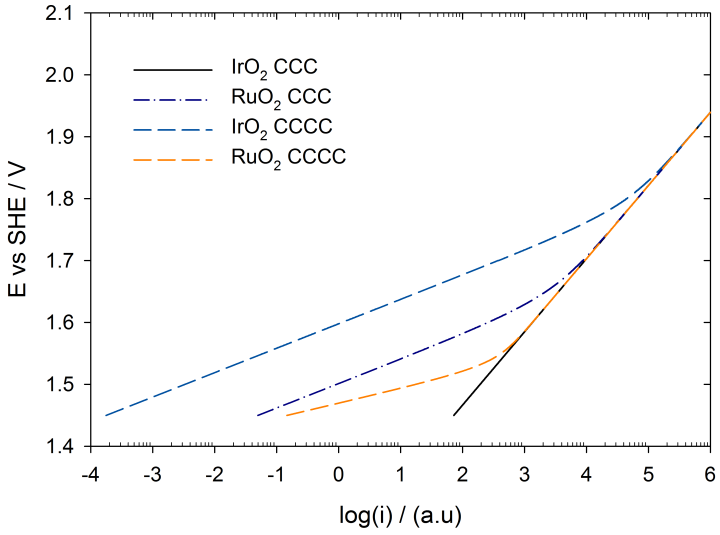

Figure 11: Simulated polarization curves based on Equations (46) and (47) and Equations (48) through (50) with $\Delta E_O = 1.66$ eV for IrO_2 and $\Delta E_O = 2.66$ eV for RuO_2. The curves were simulated for pH 0.

the DFT calculations of Rossmeisl *et al.* [6] we will have to assume that Eq. (33) represents a limiting form of Eq. (46) for RuO_2 and (47) for IrO_2.

The properties of Eq. (32) can be used to limit the number of possible de-coupled mechanisms also. For example, for a model based on Eq. (32) to comply with the experimental results the model equation will have to include a term of type $k_i^0 \exp\left[(1-\alpha_i)\, F(E-E^0)/RT\right]$ in the numerator and a term proportional to $a_{H^+} \exp\left[-F(E-E^0)/RT\right]$ in the denominator. The first requirement dictates the *rds* to be either E or C, and rules out any combination ending with a P, c.f. Table 1. Any further scrutiny will depend on quantitative assessment of the various factors on the denominator of Eq. (32), and as such data are not currently available we leave them out of the current analysis. However, the results presented here do demonstrate that a combination of experiments performed at different pH and fitting the results to quantitative models can serve to reduce substantially the number of possible mechanisms for the OER.

5.4. Effects of degradation on parameter determination

As demonstrated in Fig. 9 the IrO_2 and Ir60 samples did not suffer any noticeable degradation during the LSV measurements. For an independent assessment of the stability of iridium oxide the reader may also want to compare the forward and backward sweeps in the OER region Figures 3a and 5 in Ref. [24] for an assessment. These data indicate a deviation in the forward and backward sweep which would correspond to a maximum error of approximately 0.1 in the reaction order determined from them (calculated from formulas in Ref. [32, pp. 656–657] and assuming the deviation between forward and reverse sweeps in [24] to represent the error in the current). Also, the Tafel slopes and and transition potentials are unaffected in the curves in this reference [24], and the analysis above is valid.

Although the RuO_2 and Ir30 samples did degrade during the LSV measurements, Fig. 9, we consider the estimates of reaction order and Tafel slope to be robust with respect to such changes in the catalyst. For RuO_2 the charge after the LSV is approximately 50% of that before. Assuming a corresponding loss of area this would correspond to a shift in $\log i \sim -0.3$. Since the major part of the catalyst loss is expected to appear in the high-potential region, in the low-potential region, from which we determined the reaction order, the catalyst is likely to be much less affected. Also, Eq. (39) shows that the measurements performed here are in principle redundant. The constancy of the Tafel slope, Fig. 8(a) therefore implies a constant reaction order through Eq. (39). Since this is in excellent agreement with the experimental results in Fig. 10 for the reaction order in the low-potential region, we conclude that the measurements are consistent and the analysis not influenced significantly by instability, even for RuO_2, the sample most prone to degradation.

Also, we note in passing that recent literature indicates that the OER and the dissolution processes may share a reaction intermediate [60, 61, 62]. It therefore follows that the degradation process may follow the same current-voltage characteristics as those for the OER itself. In this case the dissolution and the OER processes will be indistinguishable, and the conclusions in terms of the reaction mechanism will remain the same unless the degradation is so severe as to cause significant changes in the surface area during the measurement.

Also our data analysis in terms of Eq. (1) gave reaction orders and Tafel slopes very similar to those above, in turn in excellent agreement with graphical estimates in the low-potential region, c.f. Fig. 6.

6. Conclusions

The polarization curves recorded as function of pH in the range 0 – 3 for $Ir_xRu_{1-x}O_2$ powders x=1, 0.6, 0.3 and 0 synthesized by the hydrolysis method could be well described by an equation derived assuming a series of concerted electron-proton transfer reaction (mononuclear reaction mechanism) with second step, the oxidation of adsorbed hydroxyl ions, being the *rds*. However, fits of the polarization data for RuO_2 were difficult to obtain in the higher potential region. This is believed to be caused by instabilities of ruthenium oxide at higher potentials. Attempts of fitting the polarization curves under the assumption that the oxide path was the appropriate mechanism resulted in substantially inferior fits. The same mechanism as for the other compositions is therefore believed to be valid also for ruthenium oxide. However, the experimental results are only consistent with DFT results if the apparent compliance with the second step of the mononuclear path being *rds* (CC model) is interpreted as representing a limiting case for the mononuclear path with the third step being the *rds* for RuO_2 and the fourth for IrO_2.

Reaction orders of protons were found for all compositions by extrapolation of the low Tafel region, and resulted in values in the range of -1.5 to -1.2. The deviation from a reaction order of -1 and the obtained fractional orders are expected if the current expression is corrected for double layer effects.

Fits to the experimental polarization curves of iridium- and ruthenium-based catalysts without invoking ohmic resistance beyond that compensated for by the potentiostat, for example an additional resistance due to bubble formation, gave results consistent the theory in terms of composition, pH and potential dependence. The work thus demonstrates the advantages of including the full expression current-potential expression when interpreting polarization curves since this utilizes information in the entire potential range.

Acknowledgements

The authors acknowledge the financial support from the Norwegian University of Science and Tehcnology (NTNU) (project no. 81730900).

References

[1] H. L. D. Bessarabov H. Wang, N. Zhao (Eds.), PEM Electrolysis for Hydrogen Production: Principles and Applications, Taylor & Francis, 2015.

[2] M. Carmo, D. L. Fritz, J. M. Mergel, D. Stolten, A comprehensive review on PEM water electrolysis, International Journal of Hydrogen Energy 38 (12) (2013) 4901 – 4934. doi:http://dx.doi.org/10.1016/j.ijhydene.2013.01.151.
URL http://www.sciencedirect.com/science/article/pii/S0360319913002607

[3] R. Parsons, Volcano curves in electrochemistry, in: E. Santos, W. Schmickler (Eds.), Catalysis in electrochemistry. From fundamentals to strategies for fuel cell development, John Wiley & Sons, 2011, Ch. 1, pp. 1–15.

[4] P. Rüetschi, P. Delahay, Influence of electrode material on oxygen overvoltage: A theoretical analysis, J. Chem. Phys. 23 (1955) 556 – 560.

[5] S. Trasatti, Electrocatalysis by oxides - Attempt at a unifying approach, Journal of Electroanalytical Chemistry and Interfacial Electrochemistry 111 (1) (1980) 125 – 131. doi:http://dx.doi.org/10.1016/S0022-0728(80)80084-2.
URL http://www.sciencedirect.com/science/article/pii/S0022072880800842

[6] J. Rossmeisl, Z.-W. Qu, H. Zhu, G.-J. Kroes, J. Nørskov, Electrolysis of water on oxide surfaces, Journal of Electroanalytical Chemistry 607 (2007) 83 – 89. doi:10.1016/j.jelechem.2006.11.008.
URL http://www.sciencedirect.com/science/article/pii/S0022072806006371

[7] J. Suntivich, K. J. May, H. A. Gasteiger, J. B. Goodenough, Y. Shao-Horn, A perovskite oxide optimized for oxygen evolution catalysis from molecular orbital principles, Science 334 (2011) 1383–1385.

[8] E. Fabbri, A. Habereder, K. Waltar, R. Kotz, T. J. Schmidt, Developments and perspectives of oxide-based catalysts for the oxygen evolution reaction, Catal. Sci. Technol. 4 (2014) 3800–3821. doi:10.1039/C4CY00669K.
URL http://dx.doi.org/10.1039/C4CY00669K

[9] R. Kötz, S. Stucki, Stabilization of RuO_2 by IrO_2 for anodic oxygen evolution in acid media, Electrochimica Acta 31 (10) (1986) 1311 – 1316. doi:10.1016/0013-4686(86)80153-0.
URL http://www.sciencedirect.com/science/article/pii/0013468686801530

[10] L.-E. Owe, M. Tsypkin, K. S. Wallwork, R. G. Haverkamp, S. Sunde, Iridium-ruthenium single phase mixed oxides for oxygen evolution: Composition dependence of electrocatalytic activity, Electrochimica Acta 70 (0) (2012) 158 – 164. doi:10.1016/j.electacta.2012.03.041.
URL http://www.sciencedirect.com/science/article/pii/S0013468612003805

[11] N. Danilovic, R. Subbaraman, K. Chang, S. Chang, Y. Kang, J. Snyder, A. Paulikas, D. Strmcnik, Y. Kim, D. Myers, V. Stamenkovic, N. Markovic, Using surface segregation to design stable Ru-Ir oxides for the oxygen evolution reaction in acidic environments, Angewandte Chemie - International Edition 53 (51) (2014) 14016–14021. doi:10.1002/anie.201406455.
URL http://www.scopus.com/inward/record.url?eid=2-s2.0-84917706702&partnerID=40&md5=341aab2b6b412ac6a296a3ff1de516de

[12] J. O. Bockris, Kinetics of Activation Controlled Consecutive Electrochemical Reactions: Anodic Evolution of Oxygen, The Journal of Chemical Physics 24 (4) (1956) 817–827. doi:http://dx.doi.org/10.1063/1.1742616.
URL http://scitation.aip.org/content/aip/journal/jcp/24/4/10.1063/1.1742616

[13] A. Damjanovic, A. Dey, J. O. Bockris, Electrode Kinetics of Oxygen Evolution and Dissolution on Rh, Ir, and Pt-Rh Alloy Electrodes, Journal of The Electrochemical Society 113 (7) (1966) 739–746.

[14] I. C. Man, Theoretical study of Electro-catalysts for oxygen evolution, Ph.D. thesis, Technical University of Denmark (DTU) (2011).

[15] I. C. Man, H.-Y. Su, F. Calle-Vallejo, H. A. Hansen, J. I. Martínez, N. G. Inoglu, J. Kitchin, T. F. Jaramillo, J. K. Nørskov, J. Rossmeisl, Universality in oxygen evolution electrocatalysis on oxide surfaces, ChemCatChem 3 (7) (2011) 1159–1165. doi:10.1002/cctc.201000397.

[16] P. Ferrin, A. U. Nilekar, J. Greeley, M. Mavrikakis, J. Rossmeisl, Reactivity descriptors for direct methanol fuel cell anode catalysts, Surf. Sci. 602 (21) (2008) 3424–3431. doi:10.1016/j.susc.2008.08.011.

[17] G. A. Tritsaris, J. Rossmeisl, Methanol Oxidation on Model Elemental and Bimetallic Transition Metal Surfaces, J. Phys. Chem. C 116 (22) (2012) 11980–11986. doi:10.1021/jp209506d.

[18] J. K. Nørskov, J. Rossmeisl, A. Logadóttir, L. Lindqvist, J. R. Kitchin, T. Bligaard, H. Jónsson, Origin of the Overpotential for Oxygen Reduction at a Fuel-Cell Cathode, J. Phys. Chem. B 108 (46) (2004) 17886–17892. doi:10.1021/jp047349j.

[19] M. T. M. Koper, Theory of multiple proton-electron transfer reactions and its implications for electrocatalysis, Chem. Sci. 4 (2016) 2710–2723. doi:10.1039/c3sc50205h.

[20] A. A. Peterson, L. C. Grabow, T. P. Brennan, B. Shong, C. Ooi, D. M. Wu, C. W. Li, A. Kushwaha, A. J. Medford, F. Mbuga, L. Li, J. K. Nørskov, Finite-Size Effects in O and CO Adsorption for the Late Transition Metals, Top. Cat. 55 (19) (2012) 1276–1282. doi:10.1007/s11244-012-9908-x.

[21] L. Giordano, B. Han, M. Risch, R. R. R. Wesley T. Hong, K. A. Stoerzinger, Y. Shao-Horn, pH dependence of OER activity of oxides: Current and future perspectives, Catalysis Today 262 (2016) 2–10. doi:http://dx.doi.org/10.1016/j.cattod.2015.10.006.

[22] R. Parsons, Manual of symbols and terminology for physicochemical quantities and units, International union of pure and applied chemistry, appendix III. Electrochemical nomenclature (1973).

[23] R. Parsons, Electrode reaction orders, transfer coefficients and rate constants - amplification of definitions and recommendations for publication of parameters, Electrochimica Acta 26 (1981) 1867–1874.

[24] E. Kuznetsova, A. Cuesta, M. Thomassen, S. Sunde, Identification of the byproducts of the oxygen evolution reaction on Rutile-type oxides under dynamic conditions, Journal of Electroanalytical Chemistry 728 (2014) 102–111. doi:10.1016/j.jelechem.2014.06.031.
URL http://www.scopus.com/inward/record.url?eid=2-s2.0-84904968105&partnerID=40&md5=55dcb617fd4a0420dd0d5fc7ea0409d6

[25] A. Reksten, F. Moradi, F. Seland, S. Sunde, Iridium-ruthenium Mixed Oxides for Oxygen Evolution Reaction Prepared by Pechini Synthesis, ECS Transactions 58 (25) (2013) 39–50.

[26] T. J. Schmidt, H. A. Gasteiger, G. D. Stb, P. M. Urban, D. M. Kolb, R. J. Behm, Characterization of High Surface Area Electrocatalysts Using a Rotating Disk Electrode Configuration, Jornal of the Electrochemical Society 145 (1998) 2354–2358.

[27] L.-E. Owe, M. Tsypkin, S. Sunde, The effect of phosphate on iridium oxide electrochemistry, Electrochimica Acta 58 (2011) 231 – 237. doi:http://dx.doi.org/10.1016/j.electacta.2011.09.043.
URL http://www.sciencedirect.com/science/article/pii/S0013468611014241

[28] K. B. Oldham, J. C. Myland, A. M. Bond, Electrochemical Science and Technology: Fundamentals and Applications, John Wiley & Sons, Ltd, 2011, Ch. Appendix, pp. 365–392. doi:10.1002/9781119965992.app1.
URL http://dx.doi.org/10.1002/9781119965992.app1

[29] A. J. Bard, L. R. Faulkner, Electrochemical Methods Fundamentals and Application, 2nd Edition, Wiley, 2001, Ch. 13, p. 72.

[30] S. Ardizzone, G. Fregonara, S. Trasatti, "Inner" and "outer" active surface of RuO_2 electrodes, Electrochimica Acta 35 (1) (1990) 263–267.
URL http://www.scopus.com/inward/record.url?eid=2-s2.0-0001224630&partnerID=40&md5=90bc47227c6ad84a4c450a60fd30e17a

[31] https://se.mathworks.com/products/matlab.html.

[32] W. T. V. W. H. Press, S. A. Teukolsky, B. P. Flannery, Numerical recipes in Fortran, Cambrige University Press, 1992.

[33] K. B. Oldham, J. C. Myland, A. M. Bond (Eds.), Electrochemical Science and Technology. Fundamentals and Applications, John Wiley & Sons, Chichester, 2012.

[34] B. E. Conway, M. A. Sattar, D. Gilroy, Electrochemistry of the Nickel-oxide Electrode-V. Self-passivation Effects in Oxygen-Evolution Kinetics, Electrochimica Acta 14 (1969) 677–694.

[35] M. E. G. Lyons, L. D. Burke, Mechanism of oxygen reactions at porous oxide electrodes, J. Chem. Soc., Faraday Trans. 1 83 (1987) 299–321.

[36] M. E. G. Lyons, L. D. Burke, Enhanced Oxygen Evolution at an Activated Iron Electrode in Alkaline Solution, J. Electroanal. Chem. 170 (1984) 377–381.

[37] I. Godwin, R. Doyle, M. Lyons, The mechanism of oxygen reactions at porous oxide electrodes III. Water oxidation catalysis at RuO2/NiO

mixed oxide electrodes, Journal of the Electrochemical Society 161 (9) (2014) F906–F917. doi:10.1149/2.0761409jes.
URL http://www.scopus.com/inward/record.url?eid=2-s2.0-84904880465&partnerID=40&md5=5cd68aa973dfd692152b2b685dcd473b

[38] B. V. Tilak, B. E. Conway, Analytical Relations between Reaction Order and Tafel Slope Derivatives for Electrocatalytic Reactions involving Chemisorbed Intermediates, Electrochimica Acta 37 (1992) 51–61.

[39] A. T. Marshall, L. Vaisson-Béthune, Avoid the quasi-equilibrium assumption when evaluating the electrocatalytic oxygen evolution reaction mechanism by Tafel slope analysis, Electrochemistry Communications 61 (2015) 23 – 26. doi:http://dx.doi.org/10.1016/j.elecom.2015.09.019.
URL http://www.sciencedirect.com/science/article/pii/S1388248115002635

[40] S. A. Akhade, J. R. Kitchin, Effects of strain, d-band filling, and oxidation state on the surface electronic structure and reactivity of 3d perovskite surfaces, J. Chem. Phys. 137 (2012) 084703–1 – 084703–9. doi:10.1063/1.4746117.

[41] A. Ruban, B. Hammer, P. Stoltze, H. Skriver, J. Nørskov, Surface electronic structure and reactivity of transition and noble metals, Journal of Molecular Catalysis A: Chemical 115 (3) (1997) 421 – 429. doi:http://dx.doi.org/10.1016/S1381-1169(96)00348-2.
URL http://www.sciencedirect.com/science/article/pii/S1381116996003482

[42] L. Ouattara, S. Fierro, O. Frey, M. Koudelka, C. Comninellis, Electrochemical comparison of IrO_2 prepared by anodic oxidation of pure iridium and IrO_2 prepared by thermal decomposition of H_2IrCl_6 precursor solution, J. Appl. Electrochem. 39 (2009) 1361–1367.

[43] J.-M. Hu, J.-Q. Zhang, C.-N. Cao, Oxygen evolution reaction on IrO_2-based DSA type electrodes: Kinetics analysis of tafel lines and EIS, International Journal of Hydrogen Energy 29 (8) (2004) 791–797. doi:10.1016/j.ijhydene.2003.09.007.
URL http://www.scopus.com/inward/record.url?eid=2-s2.0-1642339026&partnerID=40&md5=e1dcfe54f3b4bdf6910ec61532fc94eb

[44] S. Ferro, D. Rosestolato, C. A. Martinez-Huitle, A. D. Battisti, On the oxygen evolution reaction at IrO_2-SnO_2 mixed-oxide electrodes, Electrochimica Acta 146 (2014) 257 – 261. doi:http://dx.doi.org/10.1016/j.electacta.2014.08.110.
URL http://www.sciencedirect.com/science/article/pii/S0013468614018040

[45] S. Gottesfeld, S. Srinivasan, Electrochemical and Optical Studies of Thick Oxide Layers on Iridium Oxide and their Electrocatalytic Activities for the Oxygen Evolution Reaction, J. Electroanal. Chem. 86 (1978) 89–104.

[46] A. Marshall, R. Haverkamp, Electrocatalytic activity of IrO_2-RuO_2 supported on Sb-doped SnO_2 nanoparticles, Electrochimica Acta 55 (6) (2010) 1978–1984. doi:10.1016/j.electacta.2009.11.018.

[47] E. Mayousse, F. Maillard, F. Fouda-Onana, O. Sicardy, N. Guillet, Synthesis and characterization of electrocatalysts for the oxygen evolution in PEM water electrolysis, International Journal of Hydrogen Energy 36 (17) (2011) 10474 – 10481. doi:http://dx.doi.org/10.1016/j.ijhydene.2011.05.139.
URL http://www.sciencedirect.com/science/article/pii/S0360319911013887

[48] T. Reier, D. Teschner, T. Lunkenbein, A. Bergmann, S. Selve, R. Kraehnert, R. Schlgl, P. Strasser, Electrocatalytic oxygen evolution on iridium oxide: Uncovering catalyst-substrate interactions and active iridium oxide species, Journal of the Electrochemical Society 161 (9) (2014) F876–F882. doi:10.1149/2.0411409jes.
URL http://www.scopus.com/inward/record.url?eid=2-s2.0-84904891913&partnerID=40&md5=f4773df334d4bc5a6a3b0cec6b3ce501

[49] K. A. Stoerzinger, L. Qiao, M. D. Biegalski, Y. Shao-Horn, Orientation-Dependent Oxygen Evolution Activities of Rutile IrO_2 and RuO_2, Phys. Chem. Lett. 5 (2014) 1636–1641.

[50] M. V. ten Kortenaar, J. F. Vente, D. J. W. Ijdo, S. Müller, R. Kötz, Oxygen evolution and reduction on iridium oxide compounds, J. Power Sources 56 (1995) 51–60.

[51] J. Xu, G. Liu, J. Li, X. Wang, The electrocatalytic properties of an IrO_2/SnO_2 catalyst using SnO_2 as a support and an assisting reagent for the oxygen evolution reaction, Electrochimica Acta 59 (2012) 105–112.

[52] M. Yagi, E. Tomita, T. Kuwabara, Remarkably high activity of electrodeposited IrO_2 film for electrocatalytic water oxidation, J. Electroanal. Chem. 579 (2005) 83–88.

[53] C. P. D. Pauli, S. Trasatti, Composite materials for electrocatalysis of o_2 evolution: IrO_2/SnO_2 in acid solution, J. Electroanal. Chem. 538–539 (2002) 145 – 151.

[54] M. E. G. Lyons, S. Floquet, Mechanism of oxygen reactions at porous oxide electrodes. Part 2Oxygen evolution at RuO_2, IrO_2 and $Ir_xRu_{1-x}O_2$ electrodes in aqueous acid and alkaline solution, Phys. Chem. Chem. Phys. 13 (2011) 5314–5335.

[55] M. Lyons, R. Doyle, D. Fernandez, I. Godwin, M. Browne, A. Rovetta, The mechanism and kinetics of electrochemical water oxidation at oxidized metal and metal oxide electrodes. Part 2. the surfaquo group mechanism: A mini review, Electrochemistry Communications 45 (2014) 56–59. doi:10.1016/j.elecom.2014.04.019.
URL http://www.scopus.com/inward/record.url?eid=2-s2.0-84901776198&partnerID=40&md5=c6c9d3cc871ff52fac2b8f0a8227caab

[56] C. Angelinetta, M. Falciola, S. Trasatti, Heterogenous acid-base equilibria and reaction order of oxygen evolution on oxide electrodes, Journal of Electroanalytical Chemistry 205 (1-2) (1986) 347–353. doi:10.1016/0022-0728(86)90248-2.
URL http://www.scopus.com/inward/record.url?eid=2-s2.0-0000630752&partnerID=40&md5=f1ef9d3f198b78fc09322346b0f10c10

[57] A. Carugati, G. Lodi, S. Trasatti, Fractional reaction orders in oxygen evolution from acidic solutions at ruthenium oxide anodes, Materials Chemistry 6 (4-5) (1981) 255–266. doi:10.1016/0390-6035(81)90052-3.
URL http://www.scopus.com/inward/record.url?eid=2-s2.0-0342977082&partnerID=40&md5=596d0c5e06e0736c9bffd66a1eca60e1

[58] R. Doyle, M. Lyons, Kinetics and mechanistic aspects of the oxygen evolution reaction at hydrous iron oxide films in base, Journal of the Electrochemical Society 160 (2) (2013) H142–H154. doi:10.1149/2.015303jes.
URL http://www.scopus.com/inward/record.url?eid=2-s2.0-84875474971&partnerID=40&md5=1840eaef854f6168d38512961a9a4888

[59] S. Trasatti, Surface Chemistry of Oxides and Electrocatalysis, Croatica Chemica Acta (1990) 313–329.
[60] C. Spöri, J. T. H. Kwan, A. Bonakdarpour, D. P. Wilkinson, P. Strasser, The Stability Challenges of Oxygen Evolving Catalysts: Towards a Common Fundamental Understanding and Mitigation of Catalyst Degradation, Angew. Chem. Int. Ed. 56 (2017) 5994–6021. doi:10.1002/anie.201608601.
[61] S. Cherevko, S. Geiger, O. Kasian, A. Mingers, K. J. J. Mayrhofer, Oxygen evolution activity and stability of iridium in acidic media. Part 2. - Electrochemically grown hydrous iridium oxide, J. Electroanal. Chem. 774 (2016) 102–110. doi:10.1016/j.jelechem.2016.05.015.
[62] T. Binninger, R. Mohamed, K. Waltar, E. Fabbri, P. Levecque, R. Kötz, T. J. Schmidt, Thermodynamic explanation of the universal correlation between oxygen evolution activity and corrosion of oxide catalysts, Sci. Rep. 5 (2015) 12167–1–12167–7. doi:10.1038/srep12167.